




Aerial physical interaction via IDA-PBC

Burak Yüksel¹, Cristian Secchi², Heinrich H. Bühlhoff¹ and Antonio Franchi³ 

The International Journal of
Robotics Research
2019, Vol. 38(4) 403–421
© The Author(s) 2019
Article reuse guidelines:
sagepub.com/journals-permissions
DOI: 10.1177/0278364919835605
journals.sagepub.com/home/ijr



Abstract

This paper proposes the use of a novel control method based on interconnection and damping assignment–passivity-based control (IDA-PBC) in order to address the aerial physical interaction (APhI) problem for a quadrotor unmanned aerial vehicle (UAV). The apparent physical properties of the quadrotor are reshaped in order to achieve better APhI performances, while ensuring the stability of the interaction through passivity preservation. The robustness of the IDA-PBC method with respect to sensor noise is also analyzed. The direct measurement of the external wrench, needed to implement the control method, is compared with the use of a nonlinear Lyapunov-based wrench observer and advantages/disadvantages of both methods are discussed. The validity and practicability of the proposed APhI method is evaluated through experiments, where for the first time in the literature, a lightweight all-in-one low-cost force/torque (F/T) sensor is used onboard of a quadrotor. Two main scenarios are shown: a quadrotor responding to external disturbances while hovering (physical human–quadrotor interaction), and the same quadrotor sliding with a rigid tool along an uneven ceiling surface (inspection/painting-like task).

Keywords

aerial physical interaction, aerial robotics, IDA-PBC, passivity-based control, F/T sensors

1. Introduction

Aerial physical interaction (APhI) is the field in which a flying robot maintains stable flight while physically interacting with the environment. This is performed from the physics point of view by exerting meaningful forces and torques (wrenches) from the robot side to the environment, while the flying robot is accepting the wrench reactions in a stable and desired way.

Robots with flying capabilities, or aerial robots, are appealing platforms for many researchers and engineers because of their vast workspace (see Cai et al., 2014). In particular, those with stationary flight capacity, e.g., the vertical take-off and landing (VTOL) vehicles, are progressively finding use in robotic tasks (e.g., helicopters as in Naldi (2008) or ducted-fan designs as in Naldi et al. (2010)). VTOL robots provide the convenience of hovering around a fixed position, unlike fixed-wing aerial robots, which require high cruise velocities for stable flight. This ability of VTOL robots makes them suitable platforms to be used for APhI or aerial manipulation tasks.

Quadrotors are one of the most cherished and preferred VTOL designs in the literature, primarily due to their symmetric design, simple mechanics, and broad availability. Four symmetrically aligned pairwise counter-rotating

propellers allow quadrotors to move in 3D space, which at the same time makes them underactuated systems. Although underactuation is a challenge for control of the mechanical systems (see Fantoni and Lozano, 2002; Spong, 1998), it has certain benefits, e.g., it paves the way to low-weight and reduced-energy designs. In particular, thanks to the underactuation, quadrotors can swiftly accelerate along the translational directions, hence perform agile motions (see Mahony et al., 2016).

Aerial robots are used for many robotic tasks, e.g., for surveillance, monitoring, filming, etc. All these tasks have at least one thing in common: they avoid obstacles, hence a physical interaction with their environment. Recently the need for APhI has emerged, where the flying robot is expected to exert meaningful wrenches to its environment while being resilient to the counter-wrenches (reactions) in

¹Max Planck Institute for Biological Cybernetics, Tübingen, Germany

²University of Modena and Reggio Emilia, Reggio Emilia, Italy

³LAAS-CNRS, Université de Toulouse, CNRS, Toulouse, France

Corresponding author:

Burak Yüksel, Max Planck Institute for Biological Cybernetics, Spemanstr. 38, 72076, Tübingen, Germany.
Email: burak.yueksel@tuebingen.mpg.de

a stable and desired way. Since few years different methods and designs for addressing this non-trivial problem have been developed. Augugliaro and D'Andrea (2013) presented an admittance control framework allowing quadrotors to interact with humans physically. The controller presented there is proposed for the partially linearized translational dynamics in near-hovering configuration of the robot, which provides a local solution in terms of physical interaction. A hybrid position and wrench control for quadrotors was presented by Bellens et al. (2012), where for dealing with poorly structured environment, an impedance control has been exploited. Gioioso et al. (2014) turned a standard near-hovering controller into a 3D force controller, and implemented it on a quadrotor for effectively exerting desired forces to its environment via a rigid tool. Using quadrotors equipped with rigid tools for APhI was further studied by Ha et al. (2015) and Nguyen and Lee (2013), where the nonlinear quadrotor dynamics is exploited for performing tool operations, e.g., screw-driving. Fumagalli et al. (2012b) presented the design of a quadrotor VTOL robot for contact inspection purposes. The controller presented there is a *passivity-based* controller; shaping the potential energy of the quadrotor for setting a desired stiffness behavior (see also Mersha et al., 2011).

Developing controllers for nonlinear systems, which are enjoying the *passivity* property, has been one of the most evident methods in the field of control theory (for more details on passivity and how it relates to the stability of the linear/nonlinear systems, see Khalil (2001) and Sepulchre et al. (1997)). *Interconnection and damping assignment-passivity-based control* (IDA-PBC) is one of the most powerful passivity-based control methods for controlling the interactive behavior of physical systems, which allows *shaping* the energetic properties of one or interconnected multi system(s) in a power-preserving manner, such that the conservation laws of the physics are respected (see the details and its applicability in Ortega et al. (2002)). Very recently it has been adopted for controlling aerial robots as well. Acosta et al. (2014) presented control of an aerial manipulator using IDA-PBC for tracking the desired trajectories of the center of mass (CoM) of the overall system. Guerrero et al. (2015) implemented IDA-PBC for suppressing the swing of a cable attached to a quadrotor, which is carrying a load at the other end of the cable.

For the first time in the literature we have presented an IDA-PBC method for quadrotor unmanned aerial vehicles (UAVs) for performing APhI tasks in Yüksel et al. (2014b), and in Yüksel et al. (2014a) we proposed a novel wrench estimation technique to be exploited for APhI with IDA-PBC, where we have shown its effectiveness in simulations. Differently from the already existing methods, this IDA-PBC has been developed purely for quadrotors enabling them to have meaningful physical interactions with their environments for tasks, e.g., human-robot interaction or sliding, using a rigid tool for painting, cleaning, or surface inspection. This article extends our previous work in various directions by: (i) studying for the first time the

robustness of this IDA-PBC method for the quadrotor UAVs with respect to measurement noise in the form of (34) for all states and in the form of (51) for external wrench measurements; (ii) comparing experimentally the wrench estimation strategy proposed in Yüksel et al. (2014a) with a novel low-cost lightweight 6D force/torque (F/T) sensor mounted on a quadrotor; (iii) implementing for the first time a low-cost, lightweight, all-in-one F/T sensor fully onboard of a free-flying quadrotor UAV for APhI tasks; (iv) providing the first experimental results of this IDA-PBC method for demanding APhI tasks, including human-robot interaction and sliding on an uneven ceiling surface.

This article is organized as follows. In Section 2.1, we informally recall the IDA-PBC method for port-Hamiltonian (PH) systems. Then, in Section 2.2, we present the kinematics and dynamics of a quadrotor, where we rewrite its dynamics in PH form. In Section 2.3, we present the overall IDA-PBC method for quadrotor UAVs enabling them for APhI tasks. Section 2.4 is where we study the robustness of this controller against measurement noises, e.g., from sensors that are providing positions, orientations, their velocities, and the external force and torque values. In Section 3, both estimation and measurement methods of the external wrenches are presented. Here first a Lyapunov-based nonlinear external wrench observer is recalled in Section 3.1 and then in Section 3.2 we explain how to implement a lightweight all-in-one 6D Force/Torque (F/T) sensor onboard of a quadrotor. In Section 3.3, we compare the performances of these two methods over each other based on the experimental data and favor the use of F/T sensor for APhI experiments. The experimental results are provided in Section 4 for: (i) shaping the rotational inertia of a quadrotor; (ii) sliding on an uneven ceiling surface with a quadrotor equipped with a rigid tool; demonstrating the power of IDA-PBC for APhI task of the quadrotor UAVs and providing the experimental validation for our theoretical contribution.

2. IDA-PBC for quadrotors

2.1. Preliminaries on IDA-PBC

Mechanical systems can be represented as PH systems, a generalization of standard classical Hamiltonian mechanics where the energetic properties are evident. IDA-PBC is a passivity-based control strategy that allows a desired dynamics to be assigned to the controlled system that can be still represented as a PH system (see Ortega et al., 2002).

The most common representation of a PH system is as follows:

$$\begin{cases} \dot{\mathbf{x}} = [\mathcal{J}(\mathbf{x}) - \mathcal{R}(\mathbf{x})] \frac{\partial H}{\partial \mathbf{x}} + \mathbf{G}(\mathbf{x})\mathbf{u} \\ \mathbf{y} = \mathbf{G}(\mathbf{x})^T \frac{\partial H}{\partial \mathbf{x}}, \end{cases} \quad (1)$$

where $\mathbf{x} \in \mathbb{R}^n$ is the state and $H(\mathbf{x}) : \mathbb{R}^n \rightarrow \mathbb{R}_{\geq 0}$ represents the total amount of energy (*Hamiltonian*) stored in the

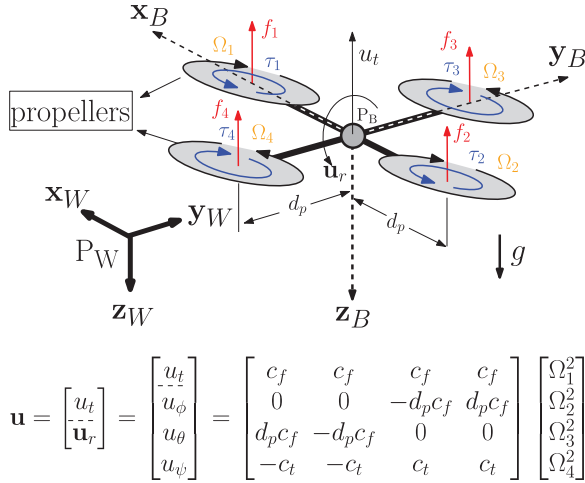


Fig. 1. A sketch of a quadrotor. Four propellers are placed symmetrically on the body frame at a distance of $d_p \in \mathbb{R}^+$ from the CoM (P_B). Each propeller rotates with a velocity $\Omega_i \in \mathbb{R}$ in opposite direction with respect to its neighbor. Owing to the design of the propellers, each of them generates a thrust force $f_i \in \mathbb{R}$ and a drag torque $\tau_i \in \mathbb{R}$. Note that these forces and torques are coupled, because $f_i = c_f \Omega_i^2$ and $\tau_i = c_t \Omega_i^2$ holds. Hence, the system is underactuated with four control inputs $\{\Omega_1, \Omega_2, \Omega_3, \Omega_4\}$, and it is trivial to find the constant mapping from these velocities to $\mathbf{u} \in \mathbb{R}^4$ of the system dynamics in Section 2.2.

system. Matrices $\mathcal{J}(\mathbf{x}) = -\mathcal{J}(\mathbf{x})^T$ and $\mathcal{R}(\mathbf{x}) \geq 0$ represent the internal energetic interconnections and the dissipation of the PH system, respectively. Furthermore, $\mathbf{G}(\mathbf{x})$ is the input matrix and the input–output pair $\langle \mathbf{u}, \mathbf{y} \rangle$ represents a power port, namely a pair of variables whose product gives the (generalized) power that is either stored or dissipated by the system. A PH system is passive with respect to the pair $\langle \mathbf{u}, \mathbf{y} \rangle$ (for more details, see, e.g., Secchi et al., 2007).

Then, using IDA-PBC from Ortega et al. (2002) and its extension proposed in Wang et al. (2009), it is possible to control a PH system in such a way that it behaves with a certain target dynamics, i.e., like a new PH system with a desired interconnection matrix, damping matrix, and energy function, and even with a different state variable $\bar{\mathbf{x}} \in \mathbb{R}^n$. As reported in Yüksel et al. (2014b), let

$$\mathbf{x} = \Phi(\bar{\mathbf{x}}, t) \quad (2)$$

be the map relating $\bar{\mathbf{x}}$ and \mathbf{x} , where Φ and $\frac{\partial \Phi}{\partial \bar{\mathbf{x}}}$ are invertible at any time t . Let $\mathcal{J}_d, \mathcal{R}_d$, and H_d be the desired interconnection matrix, dissipation matrix, and energy function, respectively. The PH system in (1) can be transformed into the target PH dynamics described by

$$\dot{\bar{\mathbf{x}}} = [\mathcal{J}_d(\bar{\mathbf{x}}) - \mathcal{R}_d(\bar{\mathbf{x}})] \frac{\partial H_d}{\partial \bar{\mathbf{x}}} \quad (3)$$

using

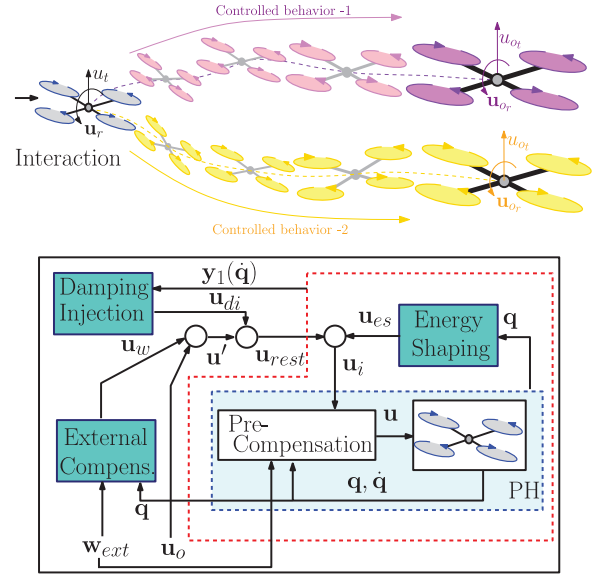


Fig. 2. Top: A sketch illustrating pictorially the idea of possibly transforming the quadrotor into two quadrotors with apparent different dynamics that react as two new physical systems to the external solicitation. Bottom: IDA-PBC controller scheme, where the pre-compensating control input is computed using (8) and all other blocks are explained in Section 2.3 in detail.

$$\mathbf{u} = \mathbf{G}^+(\mathbf{x}) \left[\frac{\partial \Phi}{\partial \bar{\mathbf{x}}} (\mathcal{J}_d(\bar{\mathbf{x}}) - \mathcal{R}_d(\bar{\mathbf{x}})) \frac{\partial H_d}{\partial \bar{\mathbf{x}}} - (\mathcal{J}(\mathbf{x}) - \mathcal{R}(\mathbf{x})) \frac{\partial H}{\partial \mathbf{x}} + \frac{\partial \Phi}{\partial t} \right], \quad (4)$$

with $\mathbf{G}^+(\mathbf{x}) = (\mathbf{G}^T(\mathbf{x})\mathbf{G}(\mathbf{x}))^{-1}\mathbf{G}^T(\mathbf{x})$ is the pseudoinverse of $\mathbf{G}(\mathbf{x})$, if and only if the following *matching equation* holds:

$$\mathbf{G}^+(\mathbf{x}) \left[\frac{\partial \Phi}{\partial \bar{\mathbf{x}}} (\mathcal{J}_d(\bar{\mathbf{x}}) - \mathcal{R}_d(\bar{\mathbf{x}})) \frac{\partial H_d}{\partial \bar{\mathbf{x}}} + \frac{\partial \Phi}{\partial t} - (\mathcal{J}(\mathbf{x}) - \mathcal{R}(\mathbf{x})) \frac{\partial H}{\partial \mathbf{x}} \right] = \mathbf{0}, \quad (5)$$

where $\mathbf{G}^+(\mathbf{x})$ is the full rank left annihilator of $\mathbf{G}(\mathbf{x})$.

2.2. Quadrotor Model and its PH Form

A sketch of a quadrotor is presented in Figure 1, where $\mathcal{F}_W : \{P_W, \mathbf{x}_W, \mathbf{y}_W, \mathbf{z}_W\}$ is the world frame, $\mathcal{F}_B : \{P_B, \mathbf{x}_B, \mathbf{y}_B, \mathbf{z}_B\}$ is the body-fixed frame whose origin P_B is the center of mass (CoM) of the quadrotor. The orientation of \mathcal{F}_B in \mathcal{F}_W is represented with a rotation matrix $\mathbf{R}(\boldsymbol{\eta}) \in \text{SO}(3)$, which is a function of $\boldsymbol{\eta} = [\phi \ \theta \ \psi]^T \in \mathbb{R}^3$ (roll–pitch–yaw angles) that is a minimal representation of the orientation. The gravity vector is facing $+\mathbf{z}_W$ and its intensity is $g \in \mathbb{R}$.

The dynamics of a quadrotor is well known (see, e.g., Yüksel et al., 2014b). The translational one can be written as

$$\Sigma_t : \{ m \ddot{\mathbf{p}}_q = -u_t \mathbf{R}(\boldsymbol{\eta}) \mathbf{e}_3 + m g \mathbf{e}_3 + \mathbf{f}_{ext}, \quad (6)$$

where $\mathbf{p}_q = [x_q \ y_q \ z_q]^T \in \mathbb{R}^3$ is the Cartesian position of P_B in \mathcal{F}_W , $m \in \mathbb{R}^+$ is the mass of the quadrotor, $u_t \in \mathbb{R}$ is the intensity of the total thrust force of the propellers acting at P_B , $\mathbf{f}_{ext} \in \mathbb{R}^3$ represents the external forces acting at P_B in \mathcal{F}_W , and $\mathbf{e}_3 = [0 \ 0 \ 1]^T$. The rotational dynamics is

$$\Sigma_r : \begin{cases} \mathbf{M}_{qr} \dot{\boldsymbol{\omega}} = [\boldsymbol{\omega}]_{\wedge} \mathbf{M}_{qr} \boldsymbol{\omega} + \mathbf{u}_r + \boldsymbol{\tau}_{ext} \\ \dot{\boldsymbol{\eta}} = \mathbf{T}(\boldsymbol{\eta}) \boldsymbol{\omega} \end{cases} \quad (7)$$

where $\mathbf{M}_{qr} \in \mathbb{R}^{3 \times 3}$ is the rotational inertia matrix, $\boldsymbol{\omega} \in \mathbb{R}^3$ is the body-frame angular velocity represented in \mathcal{F}_B , $\mathbf{T}(\boldsymbol{\eta}) \in \mathbb{R}^{3 \times 3}$ is the transformation matrix from $\boldsymbol{\omega}$ to the Euler rates $\boldsymbol{\eta}$, $\mathbf{u}_r \in \mathbb{R}^3$ is the total torque input expressed in \mathcal{F}_B , and $\boldsymbol{\tau}_{ext} \in \mathbb{R}^3$ is the total external torque. The four-dimensional control input of the quadrotor is denoted by $\mathbf{u} = [u_t \ \mathbf{u}_r^T]^T \in \mathbb{R}^4$, and the external wrench by $\mathbf{w}_{ext} = [\mathbf{f}_{ext}^T \ \boldsymbol{\tau}_{ext}^T]^T \in \mathbb{R}^6$. Finally, $[\star]_{\wedge} : \mathbb{R}^3 \rightarrow \text{so}(3)$ is the skew-symmetric operator.

For implementing the IDA-PBC on the quadrotor, we first bring the quadrotor dynamics into a PH formalization.² For this reason, we consider a pre-compensating control input (similar to that in Lee et al. (2013) and also see Figure 2) in the form of

$$\begin{aligned} \mathbf{u}_r &= \mathbf{M}_{qr} \mathbf{T}^{-1} \left[(-k_d \mathbf{I} + \mathbf{Q}) \dot{\boldsymbol{\eta}} + \ddot{\mathbf{u}}_r + (\mathbf{I} - \mathbf{M}_{qr}^{-1}) \boldsymbol{\tau}_{ext} \right] \\ \mathbf{Q} &= \mathbf{T} \dot{\mathbf{T}}^{-1} + \mathbf{T} \mathbf{M}_{qr}^{-1} [\boldsymbol{\omega}]_{\wedge} \mathbf{M}_{qr} \mathbf{T}^{-1}, \end{aligned} \quad (8)$$

where \mathbf{I} is the identity matrix with proper dimension and $k_d \in \mathbb{R}^+$. Substituting (8) in (7), we obtain

$$\dot{\boldsymbol{\eta}} = -k_d \dot{\boldsymbol{\eta}} + \ddot{\mathbf{u}}_r + \boldsymbol{\tau}_{ext}. \quad (9)$$

Hence, after the pre-compensation given in (8), the quadrotor dynamics is defined by (6) and (9). This new system can be modeled as a mechanical PH system. Let $\mathbf{M} = \text{diag}(m\mathbf{I}, \mathbf{I}) \in \mathbb{R}^{6 \times 6}$ and define $\mathbf{q} = [\mathbf{p}_q^T \ \boldsymbol{\eta}^T]^T = [q_1 \ \dots \ q_6]^T \in \mathbb{R}^6$ and $\mathbf{p} = \mathbf{M} \dot{\mathbf{q}} \in \mathbb{R}^6$ as the configuration and momentum variables, respectively. Furthermore, let $\mathbf{u}_i = [u_t \ \ddot{\mathbf{u}}_r^T]^T \in \mathbb{R}^4$ be the input vector (see Figure 2 for how \mathbf{u}_i enters the controller). The dynamics (6) and (9) can be rewritten as

$$\begin{bmatrix} \dot{\mathbf{q}} \\ \dot{\mathbf{p}} \end{bmatrix} = \left[\begin{pmatrix} \mathbf{0} & \mathbf{I} \\ -\mathbf{I} & \mathbf{0} \end{pmatrix} - \begin{pmatrix} \mathbf{0} & \mathbf{0} \\ \mathbf{0} & \mathcal{R} \end{pmatrix} \right] \begin{bmatrix} \frac{\partial H}{\partial \mathbf{q}} \\ \frac{\partial H}{\partial \mathbf{p}} \end{bmatrix} + \begin{bmatrix} \mathbf{0} & \mathbf{0} \\ \mathbf{G} & \mathbf{I} \end{bmatrix} \begin{bmatrix} \mathbf{u}_i \\ \mathbf{w}_{ext} \end{bmatrix}, \quad (10)$$

where $\mathcal{R} = k_d \mathbf{I}$ models the dissipation introduced by (8), and \mathbf{I} and $\mathbf{0}$ stand for the identity and zero matrices of proper dimensions, respectively. The total energy function and the control input matrix \mathbf{G} are given by

$$H(\mathbf{q}, \mathbf{p}) = \frac{1}{2} \mathbf{p}^T \mathbf{M}^{-1} \mathbf{p} + V(\mathbf{q}) = \frac{1}{2} \mathbf{p}^T \mathbf{M}^{-1} \mathbf{p} - mgq_3, \quad (11)$$

$$\mathbf{G} = \begin{bmatrix} \mathbf{g}_1 & \mathbf{0} \\ \mathbf{0} & \mathbf{I} \end{bmatrix} \in \mathbb{R}^{6 \times 4} \quad \text{with } \mathbf{g}_1 = -\mathbf{R}\mathbf{e}_3 \in \mathbb{R}^3. \quad (12)$$

The following proposition holds.

Proposition 1. *The system (10) is cyclo-passive with respect to the pair*

$$\left\langle \begin{bmatrix} \mathbf{u}_i \\ \mathbf{w}_{ext} \end{bmatrix}, \begin{bmatrix} \mathbf{G}^T \frac{\partial H}{\partial \mathbf{p}} \\ \frac{\partial H}{\partial \mathbf{p}} \end{bmatrix} \right\rangle.$$

Proof. Consider the energy function defined in (11). Using (10) we obtain

$$\begin{aligned} \dot{H} &= \begin{bmatrix} \frac{\partial^T H}{\partial \mathbf{q}} & \frac{\partial^T H}{\partial \mathbf{p}} \end{bmatrix} \begin{bmatrix} \dot{\mathbf{q}} \\ \dot{\mathbf{p}} \end{bmatrix} \\ &= -\frac{\partial^T H}{\partial \mathbf{p}} \mathcal{R} \frac{\partial H}{\partial \mathbf{p}} + \frac{\partial^T H}{\partial \mathbf{p}} \mathbf{G} \mathbf{u}_i + \frac{\partial^T H}{\partial \mathbf{p}} \mathbf{w}_{ext}. \end{aligned} \quad (13)$$

Considering that $\mathcal{R} \geq \mathbf{0}$ we obtain

$$\dot{H} \leq \frac{\partial^T H}{\partial \mathbf{p}} \mathbf{G} \mathbf{u}_i + \frac{\partial^T H}{\partial \mathbf{p}} \mathbf{w}_{ext} \quad (14)$$

which proves the statement. \blacksquare

Cyclo-passivity is an extension of the passivity property, which requires the system to behave as a physical system from an energetic point of view (i.e., that the energy introduced into the system from the external world is either stored or dissipated) but does not require the energy function being lower bounded. The meticulous reader can refer to Willems (1972) for more details on cyclo-passivity.

2.3. IDA-PBC framework

Now let us show how one can use IDA-PBC method for bringing the original system dynamics (10) into the desired (target) one

$$\begin{bmatrix} \dot{\mathbf{q}} \\ \dot{\bar{\mathbf{p}}} \end{bmatrix} = \left[\begin{pmatrix} \mathbf{0} & \mathbf{I} \\ -\mathbf{I} & \mathbf{0} \end{pmatrix} - \begin{pmatrix} \mathbf{0} & \mathbf{0} \\ \mathbf{0} & \mathcal{R}_d \end{pmatrix} \right] \begin{bmatrix} \frac{\partial H_d}{\partial \mathbf{q}} \\ \frac{\partial H_d}{\partial \bar{\mathbf{p}}} \end{bmatrix} + \begin{bmatrix} \mathbf{0} \\ \mathbf{I} \end{bmatrix} \bar{\mathbf{w}}_{ext}, \quad (15)$$

where $\bar{\mathbf{p}} = \mathbf{M}_d \dot{\mathbf{q}}$ is the new momentum associated to the new inertia matrix $\mathbf{M}_d = \text{diag}(m_d \mathbf{I}, \mathbf{N}) \in \mathbb{R}^{6 \times 6}$, $m_d \in \mathbb{R}^+$ is the desired mass, and $\mathbf{N} \in \mathbb{R}^{3 \times 3}$ is a positive-definite desired rotational inertia matrix. The desired energy function is

$$H_d = \frac{1}{2} \bar{\mathbf{p}}^T \mathbf{M}_d^{-1} \bar{\mathbf{p}} + V_d(\mathbf{q}), \quad (16)$$

where V_d is the desired potential energy satisfying the matching condition of IDA-PBC (see (5)). The desired dissipation matrix \mathcal{R}_d has to be designed in order to assign a desired viscous behavior to the new quadrotor dynamics, while taking its underactuation into account. Finally

$\bar{\mathbf{w}}_{ext} \in \mathbb{R}^6$ is the best external wrench compensation that can be achieved considering the underactuation of the system.

The goal of imposing the different target dynamics given in (15) is to let the system react in a different (desired) way to the external solicitations, as if it was a physically different system. Here we briefly recall the main steps for building the IDA-PBC controller for quadrotors. A more detailed description can be found in Yüksel et al. (2014b).

The IDA-PBC control input is $\mathbf{u}_i = \mathbf{u}_{es} + \mathbf{u}_{di} + \mathbf{u}_w + \mathbf{u}_o$, where the four low-level control inputs are defined as: *i)* \mathbf{u}_{es} , energy shaping input; *ii)* \mathbf{u}_{di} , damping injection input; *iii)* \mathbf{u}_w , external wrench compensation input; and *iv)* an additional high-level control input, $\mathbf{u}_o \in \mathbb{R}^4$, which can be used for, e.g., position or F/T tracking. See also Figure 2 for a sketch showing how all these control inputs are combined.

We start showing the computation of the energy shaping control input.

2.3.1. Energy shaping. Consider the original system dynamics (10) in the absence of any dissipative elements and for now not considering any external disturbances:

$$\begin{bmatrix} \dot{\mathbf{q}} \\ \dot{\mathbf{p}} \end{bmatrix} = \begin{bmatrix} \mathbf{0} & \mathbf{I} \\ -\mathbf{I} & \mathbf{0} \end{bmatrix} \begin{bmatrix} \frac{\partial H}{\partial \mathbf{q}} \\ \frac{\partial H}{\partial \mathbf{p}} \end{bmatrix} + \begin{bmatrix} \mathbf{0} \\ \mathbf{G} \end{bmatrix} \mathbf{u}_{es}, \quad (17)$$

where the input \mathbf{u}_{es} has to be designed in order to obtain an undamped controlled system with the desired energy function H_d and with the desired momentum $\bar{\mathbf{p}}$, i.e., to obtain

$$\begin{bmatrix} \dot{\mathbf{q}} \\ \dot{\mathbf{p}} \end{bmatrix} = \begin{bmatrix} \mathbf{0} & \mathbf{I} \\ -\mathbf{I} & \mathbf{0} \end{bmatrix} \begin{bmatrix} \frac{\partial H_d}{\partial \mathbf{q}} \\ \frac{\partial H_d}{\partial \bar{\mathbf{p}}} \end{bmatrix}. \quad (18)$$

It has been shown in Yüksel et al. (2014b) that for the system at hand, the map (2) relating $\mathbf{x} = [\mathbf{q}^T \mathbf{p}^T]^T$ to $\bar{\mathbf{x}} = [\bar{\mathbf{q}}^T \bar{\mathbf{p}}^T]^T$ is actually

$$\mathbf{x} = \Phi(\bar{\mathbf{x}}), \quad \Phi(\bar{\mathbf{x}}) = \mathbf{F}\bar{\mathbf{x}}, \quad \mathbf{F} = \begin{bmatrix} \mathbf{I} & \mathbf{0} \\ \mathbf{0} & \mathbf{M}\mathbf{M}_d^{-1} \end{bmatrix}, \quad (19)$$

which implies that $\frac{\partial \Phi}{\partial \bar{\mathbf{x}}} = \mathbf{F}$, and $\frac{\partial \Phi}{\partial \bar{\mathbf{t}}} = \mathbf{0}$. Under this circumstances, by choosing the energy shaping control input as

$$\mathbf{u}_{es} = \mathbf{G}^+ \left(\frac{\partial H}{\partial \mathbf{q}} - \mathbf{M}\mathbf{M}_d^{-1} \frac{\partial H_d}{\partial \mathbf{q}} \right) \quad (20)$$

we can modify the original undamped system (17) into the target dynamics (18) if and only if the matching condition given in (5) holds. In Yüksel et al. (2014b) we have shown that choosing

$$V_d(\mathbf{q}) = -m_d g q_3 + \bar{V}_d(\boldsymbol{\eta}) \quad (21)$$

is one way to meet (5), when there are no singularities in the quadrotor's configuration and $\bar{V}_d(\boldsymbol{\eta})$ is a “well-behaved”³ energetic function from physics point of view, e.g.,

$$\begin{aligned} \bar{V}_d &= \frac{1}{2} \boldsymbol{\eta}_e^T \mathbf{K}_p \boldsymbol{\eta}_e \\ \boldsymbol{\eta}_e &= \boldsymbol{\eta} - \boldsymbol{\eta}^*, \end{aligned} \quad (22)$$

where $\mathbb{R}^{3 \times 3} \ni \mathbf{K}_p > \mathbf{0}$ and the desired attitude $\boldsymbol{\eta}^* = [\phi^* \ \theta^* \ \psi^*]^T \in \mathbb{R}^3$ is an orientation equilibrium away from singularities, where the rotational potential reaches its minimum.

Now we show how one can shape the dissipative behavior of the quadrotor by using damping injection.

2.3.2. Damping injection. The IDA-PBC input can be written as $\mathbf{u}_i = \mathbf{u}_{es} + \mathbf{u}_{rest}$, where $\mathbf{u}_{rest} = \mathbf{u}_{di} + \mathbf{u}_w + \mathbf{u}_o$. In Yüksel et al. (2014b) it was shown that considering the mapping in (19) and the fact that $\frac{\partial H}{\partial \mathbf{p}} = \frac{\partial H_d}{\partial \bar{\mathbf{p}}}$, implementing the control input $\mathbf{u}_i = \mathbf{u}_{es} + \mathbf{u}_{rest}$ (considering also (20)) on the original system dynamics (10) will result in

$$\begin{aligned} \begin{bmatrix} \dot{\mathbf{q}} \\ \dot{\mathbf{p}} \end{bmatrix} &= \begin{bmatrix} \mathbf{0} & \mathbf{I} \\ -\mathbf{I} & \mathbf{0} \end{bmatrix} \begin{bmatrix} \frac{\partial H_d}{\partial \mathbf{q}} \\ \frac{\partial H_d}{\partial \bar{\mathbf{p}}} \end{bmatrix} - \begin{bmatrix} \mathbf{0} & \mathbf{0} \\ \mathbf{0} & \mathbf{M}_d \mathbf{M}^{-1} \mathcal{R} \end{bmatrix} \begin{bmatrix} \frac{\partial H}{\partial \mathbf{q}} \\ \frac{\partial H_d}{\partial \bar{\mathbf{p}}} \end{bmatrix} \\ &+ \begin{bmatrix} \mathbf{0} \\ \mathbf{M}_d \mathbf{M}^{-1} \mathbf{G} \end{bmatrix} \mathbf{u}_{rest} + \begin{bmatrix} \mathbf{0} \\ \mathbf{M}_d \mathbf{M}^{-1} \end{bmatrix} \mathbf{w}_{ext}. \end{aligned} \quad (23)$$

Now decomposing the control input $\mathbf{u}_{rest} = \mathbf{u}_{di} + \mathbf{u}'$ with $\mathbf{u}' = \mathbf{u}_w + \mathbf{u}_o$ (see Figure 2) and setting

$$\mathbf{u}_{di} = -\mathbf{K}_v \mathbf{y}_1, \quad (24)$$

where

$$\mathbf{y}_1 = \mathbf{G}^T \mathbf{M}^{-T} \mathbf{M}_d^T \frac{\partial H_d}{\partial \bar{\mathbf{p}}}, \quad \mathbf{K}_v = \begin{bmatrix} k_T & \mathbf{0} \\ \mathbf{0} & \mathbf{K}_R \end{bmatrix} \in \mathbb{R}^{4 \times 4}$$

and implementing \mathbf{u}_{di} in (23) we obtain

$$\begin{aligned} \begin{bmatrix} \dot{\mathbf{q}} \\ \dot{\mathbf{p}} \end{bmatrix} &= \left[\begin{bmatrix} \mathbf{0} & \mathbf{I} \\ -\mathbf{I} & \mathbf{0} \end{bmatrix} - \begin{bmatrix} \mathbf{0} & \mathbf{0} \\ \mathbf{0} & \mathcal{R}_d \end{bmatrix} \right] \begin{bmatrix} \frac{\partial H_d}{\partial \mathbf{q}} \\ \frac{\partial H_d}{\partial \bar{\mathbf{p}}} \end{bmatrix} \\ &+ \begin{bmatrix} \mathbf{0} \\ \mathbf{M}_d \mathbf{M}^{-1} \mathbf{G} \end{bmatrix} \mathbf{u}' + \begin{bmatrix} \mathbf{0} \\ \mathbf{M}_d \mathbf{M}^{-1} \end{bmatrix} \mathbf{w}_{ext}, \end{aligned} \quad (25)$$

where \mathcal{R}_d denotes the desired dissipation matrix, achieved via damping injection for assigning a target viscous behavior to the system.

Remark 1. The choice of $\mathbf{K}_v \in \mathbb{R}^{4 \times 4}$ in (24) has to be done in a way that the desired dissipation matrix \mathcal{R}_d in (25) is positive definite. It was shown in Yüksel et al. (2014b) that this can be achieved for $\mathbf{K}_v = \text{diag}([k_T \ \mathbf{K}_R])$, where $k_T \in \mathbb{R}^+$ and $\mathbb{R}^{3 \times 3} \ni \mathbf{K}_R > \mathbf{0}$, with

$$\begin{cases} k_T = \left(\frac{m}{m_d}\right)^2 \bar{k}_T \\ \mathbf{K}_R = \mathbf{N}^{-1} (\bar{\mathbf{K}}_R - k_d \mathbf{N}) \mathbf{N}^{-1}, \end{cases} \quad (26)$$

for any $\bar{k}_T \in \mathbb{R}^+$ and $\mathbb{R}^{3 \times 3} \ni \bar{\mathbf{K}}_R > \mathbf{0}$.

2.3.3. External wrench compensation. The change of the momentum for the desired (target) dynamics and the underactuation of the system introduces a scaling not only to the control of the system, but also to the way the external wrench \mathbf{w}_{ext} influences the evolution of the system. Ideally this wrench should influence the controlled system dynamics in the same way it does for the original system given in (10). Hence, a control action, called external wrench compensation, needs to be taken into account to eliminate this scaling. In Yüksel et al. (2014b) it was shown that this can be done by applying the following control input further in (25)

$$\begin{aligned} \mathbf{u}' &= \mathbf{u}_w + \mathbf{u}_o \\ \mathbf{u}_w &= \mathbf{G}^+ (\mathbf{M}\mathbf{M}_d^{-1}(\mathbf{I} - \mathbf{M}_d\mathbf{M}^{-1})\mathbf{w}_{ext}), \end{aligned} \quad (27)$$

which leads to the following closed-loop system

$$\begin{aligned} \begin{bmatrix} \dot{\mathbf{q}} \\ \dot{\mathbf{p}} \end{bmatrix} &= \left[\begin{pmatrix} \mathbf{0} & \mathbf{I} \\ -\mathbf{I} & \mathbf{0} \end{pmatrix} - \begin{pmatrix} \mathbf{0} & \mathbf{0} \\ \mathbf{0} & \mathcal{R}_d \end{pmatrix} \right] \begin{bmatrix} \frac{\partial H_d}{\partial \mathbf{q}} \\ \frac{\partial H_d}{\partial \mathbf{p}} \end{bmatrix} + \begin{bmatrix} \mathbf{0} \\ \mathbf{I} \end{bmatrix} \bar{\mathbf{w}}_{ext} \\ &+ \begin{bmatrix} \mathbf{0} \\ \mathbf{M}_d\mathbf{M}^{-1}\mathbf{G} \end{bmatrix} \mathbf{u}_o, \end{aligned} \quad (28)$$

that is the physically reshaped quadrotor with desired (target) dynamics. Note that for $\mathbf{u}_o = \mathbf{0}$, (28) is identical to (15).

Summarizing, the IDA-PBC control input in the form of

$$\begin{aligned} \mathbf{u}_i &= \mathbf{u}_{es} + \mathbf{u}_{di} + \mathbf{u}_w + \mathbf{u}_o \\ \mathbf{u}_{es} &= \mathbf{G}^+ \left(\frac{\partial H}{\partial \mathbf{q}} - \mathbf{M}\mathbf{M}_d^{-1} \frac{\partial H_d}{\partial \mathbf{q}} \right) \\ \mathbf{u}_{di} &= -\mathbf{K}_v \mathbf{G}^T \mathbf{M}^{-T} \mathbf{M}_d^T \frac{\partial H_d}{\partial \mathbf{p}} \\ \mathbf{u}_w &= \mathbf{G}^+ \mathbf{M}\mathbf{M}_d^{-1} (\mathbf{I} - \mathbf{M}_d\mathbf{M}^{-1}) \mathbf{w}_{ext}, \end{aligned} \quad (29)$$

brings the system described in (10) into (28), which has desired ‘‘apparent’’ physical properties.

The control loop providing \mathbf{u}_i can be considered as a *low-level* one, which is responsible for controlling the APhI, and also accepts a *high-level* control input, $\mathbf{u}_o \in \mathbb{R}^4$, which can be computed for, e.g., position or F/T tracking.

Proposition 2. *The controlled system (28) is cyclo-passive with respect to the input–output pair:*

$$\left\langle \begin{bmatrix} \mathbf{u}_o \\ \bar{\mathbf{w}}_{ext} \end{bmatrix}, \begin{bmatrix} \mathbf{G}^T \mathbf{M}^{-T} \mathbf{M}_d^T \frac{\partial H_d}{\partial \mathbf{p}} \\ \frac{\partial H_d}{\partial \mathbf{p}} \end{bmatrix} \right\rangle.$$

Proof. Consider the energy function defined in (16). Using (28) we obtain:

$$\begin{aligned} \dot{H}_d &= \begin{bmatrix} \frac{\partial^T H_d}{\partial \mathbf{q}} & \frac{\partial^T H_d}{\partial \mathbf{p}} \end{bmatrix} \begin{bmatrix} \dot{\mathbf{q}} \\ \dot{\mathbf{p}} \end{bmatrix} \\ &= -\frac{\partial^T H_d}{\partial \mathbf{p}} \mathcal{R}_d \frac{\partial H_d}{\partial \mathbf{p}} + \frac{\partial^T H_d}{\partial \mathbf{p}} \mathbf{M}_d \mathbf{M}^{-1} \mathbf{G} \mathbf{u}_o \\ &\quad + \frac{\partial^T H_d}{\partial \mathbf{p}} \bar{\mathbf{w}}_{ext}. \end{aligned} \quad (30)$$

Considering that $\mathcal{R}_d \geq \mathbf{0}$ by taking Remark 1 in to account, we obtain that

$$\dot{H}_d \leq \frac{\partial^T H_d}{\partial \mathbf{p}} \mathbf{M}_d \mathbf{M}^{-1} \mathbf{G} \mathbf{u}_o + \frac{\partial^T H_d}{\partial \mathbf{p}} \bar{\mathbf{w}}_{ext} \quad (31)$$

which proves the statement. \blacksquare

2.4. Robustness of IDA-PBC

In this section, we provide a robustness analysis of the IDA-PBC strategy presented above (considering the \mathbf{u}_i as computed in (29)) against noisy measurements.⁴ Remember that this controller consists of three steps: (i) energy shaping; (ii) damping injection; (iii) external wrench compensation. Our goal is to keep the analysis simple and isolate the effects of disturbances on the single components of the control action. Let us consider the PH formalization of the system, which is not yet damped, and in which no external wrench is apparent:

$$\begin{bmatrix} \dot{\mathbf{q}} \\ \dot{\mathbf{p}} \end{bmatrix} = \begin{bmatrix} \mathbf{0} & \mathbf{I} \\ -\mathbf{I} & \mathbf{0} \end{bmatrix} \begin{bmatrix} \frac{\partial H}{\partial \mathbf{q}} \\ \frac{\partial H}{\partial \mathbf{p}} \end{bmatrix} + \begin{bmatrix} \mathbf{0} \\ \mathbf{G} \end{bmatrix} \mathbf{u}_{es}, \quad (32)$$

where

$$\mathbf{G} = \begin{bmatrix} -\mathbf{R}(\boldsymbol{\eta})\mathbf{e}_3 & \mathbf{0} \\ \mathbf{0} & \mathbf{I} \end{bmatrix}, \quad \mathbf{G}^+ = \begin{bmatrix} -\mathbf{e}_3^T \mathbf{R}^T(\boldsymbol{\eta}) & \mathbf{0} \\ \mathbf{0} & \mathbf{I} \end{bmatrix}, \quad (33)$$

with $\mathbf{G}^+ = (\mathbf{G}^T \mathbf{G})^{-1} \mathbf{G}^T$. Consider the noisy states, which are used for computing the control inputs:

$$\begin{aligned} \tilde{\mathbf{q}} &= \begin{bmatrix} \tilde{\mathbf{p}}_q \\ \tilde{\boldsymbol{\eta}} \end{bmatrix} = \begin{bmatrix} \mathbf{p}_q \\ \boldsymbol{\eta} \end{bmatrix} + \begin{bmatrix} \mathbf{p}_{qN} \\ \boldsymbol{\eta}_N \end{bmatrix} \\ \dot{\tilde{\mathbf{q}}} &= \begin{bmatrix} \dot{\tilde{\mathbf{p}}}_q \\ \dot{\tilde{\boldsymbol{\eta}}} \end{bmatrix} = \begin{bmatrix} \dot{\mathbf{p}}_q \\ \dot{\boldsymbol{\eta}} \end{bmatrix} + \begin{bmatrix} \dot{\mathbf{p}}_{qN} \\ \dot{\boldsymbol{\eta}}_N \end{bmatrix}, \end{aligned} \quad (34)$$

where $\tilde{\mathbf{q}}$ and $\dot{\tilde{\mathbf{q}}}$ indicate the noisy measurements of the configuration and of the velocity of the quadrotor CoM. Furthermore, the terms \mathbf{p}_{qN} , $\boldsymbol{\eta}_N$, $\dot{\mathbf{p}}_{qN}$, and $\dot{\boldsymbol{\eta}}_N$ indicate the bounded noises/disturbances affecting the measurements.

2.4.1. Energy shaping analysis. For now, consider only the energy shaping control input \mathbf{u}_{es} as given in (20), which can be re-formalized as

$$\mathbf{u}_{es} = \mathbf{G}^+(\boldsymbol{\eta}) \left(\begin{bmatrix} \boldsymbol{\gamma} \\ \mathbf{0} \end{bmatrix} - \mathbf{M}\mathbf{M}_d^{-1} \begin{bmatrix} \boldsymbol{\gamma}_d \\ \nabla_{\boldsymbol{\eta}} V_d(\boldsymbol{\eta}) \end{bmatrix} \right), \quad (35)$$

where $\boldsymbol{\gamma} = [0 \ 0 \ -mg]^T \in \mathbb{R}^3$, $\boldsymbol{\gamma}_d = [0 \ 0 \ -m_d g]^T \in \mathbb{R}^3$, and $\nabla_{*} f$ denotes $\frac{\partial f}{\partial *}$.

Considering the noises in the measurements, the noisy control input becomes

$$\tilde{\mathbf{u}}_{es} = \mathbf{G}^+(\tilde{\boldsymbol{\eta}}) \left(\begin{bmatrix} \boldsymbol{\gamma} \\ \mathbf{0} \end{bmatrix} - \mathbf{M}\mathbf{M}_d^{-1} \begin{bmatrix} \boldsymbol{\gamma}_d \\ \nabla_{\tilde{\boldsymbol{\eta}}} V_d(\tilde{\boldsymbol{\eta}}) \end{bmatrix} \right). \quad (36)$$

Now, considering the last three rows of (32), we can write

$$\dot{\mathbf{p}} = -\nabla_{\mathbf{q}} H(\boldsymbol{\eta}) + \mathbf{G}(\boldsymbol{\eta})\mathbf{u}_{es} = -\begin{bmatrix} \boldsymbol{\gamma} \\ \mathbf{0} \end{bmatrix} + \mathbf{G}(\boldsymbol{\eta})\mathbf{u}_{es}. \quad (37)$$

Then, the way $\tilde{\mathbf{u}}_{es}$ affects the system in (32) is

$$\begin{aligned} \dot{\mathbf{p}} &= -\begin{bmatrix} \boldsymbol{\gamma} \\ \mathbf{0} \end{bmatrix} + \mathbf{G}(\boldsymbol{\eta})\tilde{\mathbf{u}}_{es} \\ &= -\begin{bmatrix} \boldsymbol{\gamma} \\ \mathbf{0} \end{bmatrix} + \mathbf{G}(\boldsymbol{\eta})\mathbf{u}_{es} + \mathbf{G}(\boldsymbol{\eta})(\tilde{\mathbf{u}}_{es} - \mathbf{u}_{es}). \end{aligned} \quad (38)$$

Let us compute the explicit expression of the term $\mathbf{G}(\boldsymbol{\eta})\mathbf{u}_{es}$. Considering (35) together with (33), we can say

$$\begin{aligned} \mathbf{G}(\boldsymbol{\eta})\mathbf{u}_{es} &= \mathbf{G}(\boldsymbol{\eta})\mathbf{G}^+(\boldsymbol{\eta}) \left(\begin{bmatrix} \boldsymbol{\gamma} \\ \mathbf{0} \end{bmatrix} - \mathbf{M}\mathbf{M}_d^{-1} \begin{bmatrix} \boldsymbol{\gamma}_d \\ \nabla_{\boldsymbol{\eta}} V_d(\boldsymbol{\eta}) \end{bmatrix} \right) \\ &= -\mathbf{G}(\boldsymbol{\eta})\mathbf{G}^+(\boldsymbol{\eta}) \begin{bmatrix} \mathbf{0} \\ \mathbf{N}^{-1}\nabla_{\boldsymbol{\eta}} V_d(\boldsymbol{\eta}) \end{bmatrix} \\ &= -\begin{bmatrix} \mathbf{0} \\ \mathbf{N}^{-1}\nabla_{\boldsymbol{\eta}} V_d(\boldsymbol{\eta}) \end{bmatrix}. \end{aligned} \quad (39)$$

Thus, we can write (38) as

$$\dot{\mathbf{p}} = -\begin{bmatrix} \boldsymbol{\gamma} \\ \mathbf{0} \end{bmatrix} - \begin{bmatrix} \mathbf{0} \\ \mathbf{N}^{-1}\nabla_{\boldsymbol{\eta}} V_d(\boldsymbol{\eta}) \end{bmatrix} + \mathbf{G}(\boldsymbol{\eta})(\tilde{\mathbf{u}}_{es} - \mathbf{u}_{es}). \quad (40)$$

Energy shaping control input reshapes the physics of the system by not only by assigning a desired inertia but also by changing its state from $\mathbf{p} = \mathbf{M}\dot{\mathbf{q}}$ to $\tilde{\mathbf{p}} = \mathbf{M}_d\dot{\tilde{\mathbf{q}}}$, which considering (40) leads to

$$\begin{aligned} \dot{\tilde{\mathbf{p}}} &= \mathbf{M}_d\mathbf{M}^{-1}\dot{\mathbf{p}} \\ &= -\begin{bmatrix} \boldsymbol{\gamma}_d \\ \mathbf{0} \end{bmatrix} - \begin{bmatrix} \mathbf{0} \\ \nabla_{\boldsymbol{\eta}} V_d(\boldsymbol{\eta}) \end{bmatrix} + \underbrace{\mathbf{M}_d\mathbf{M}^{-1}\mathbf{G}(\boldsymbol{\eta})}_{\mathbf{w}_{es}}(\tilde{\mathbf{u}}_{es} - \mathbf{u}_{es}), \end{aligned} \quad (41)$$

where \mathbf{w}_{es} is the wrench due to the effect of the noisy state disturbance to the energy shaping control input. Recalling from (39) that

$$\begin{aligned} \mathbf{G}(\boldsymbol{\eta})\mathbf{u}_{es} &= -\begin{bmatrix} \mathbf{0} \\ \mathbf{N}^{-1}\nabla_{\boldsymbol{\eta}} V_d(\boldsymbol{\eta}) \end{bmatrix} \\ \mathbf{G}(\boldsymbol{\eta})\tilde{\mathbf{u}}_{es} &= -\begin{bmatrix} \mathbf{0} \\ \mathbf{N}^{-1}\nabla_{\tilde{\boldsymbol{\eta}}} V_d(\tilde{\boldsymbol{\eta}}) \end{bmatrix} \end{aligned}$$

and placing them in \mathbf{w}_{es} shown in (41), we can explicitly compute the effect of the disturbance as

$$\begin{aligned} \mathbf{w}_{es} &= \mathbf{M}_d\mathbf{M}^{-1} \left(\begin{bmatrix} \mathbf{0} \\ \mathbf{N}^{-1}\nabla_{\boldsymbol{\eta}} V_d(\boldsymbol{\eta}) \end{bmatrix} - \begin{bmatrix} \mathbf{0} \\ \mathbf{N}^{-1}\nabla_{\tilde{\boldsymbol{\eta}}} V_d(\tilde{\boldsymbol{\eta}}) \end{bmatrix} \right) \\ &= \begin{bmatrix} \mathbf{0} \\ \nabla_{\boldsymbol{\eta}} V_d(\boldsymbol{\eta}) \end{bmatrix} - \begin{bmatrix} \mathbf{0} \\ \nabla_{\tilde{\boldsymbol{\eta}}} V_d(\tilde{\boldsymbol{\eta}}) \end{bmatrix}. \end{aligned} \quad (42)$$

Now, for a desired energy in the form of (21) and (22), we can say that $\nabla_{\boldsymbol{\eta}} V_d(\boldsymbol{\eta}) = \mathbf{K}_p\boldsymbol{\eta}$ and $\nabla_{\tilde{\boldsymbol{\eta}}} V_d(\tilde{\boldsymbol{\eta}}) = \mathbf{K}_p\tilde{\boldsymbol{\eta}}$. In addition, recalling from (34) that $\tilde{\boldsymbol{\eta}} = \boldsymbol{\eta} + \boldsymbol{\eta}_N$, we can write \mathbf{w}_{es} in (42) as

$$\mathbf{w}_{es} = \begin{bmatrix} \mathbf{0} \\ -\mathbf{K}_p\boldsymbol{\eta}_N \end{bmatrix}. \quad (43)$$

Thus, we can conclude that the effect of the noisy states on the energy shaping step is given by a bounded torque only and it does not generate disturbing forces for the translational dynamics.

2.4.2. Damping injection analysis. A similar analysis can be done for the damping injection. From (24) we have that

$$\begin{aligned} \mathbf{u}_{di} &= \mathbf{S}(\boldsymbol{\eta})\dot{\mathbf{q}}, \\ \mathbf{S}(\boldsymbol{\eta}) &= -\mathbf{K}_V\mathbf{G}^T(\boldsymbol{\eta})\mathbf{M}^{-T}\mathbf{M}_d^T \\ \mathbf{K}_V &= \begin{bmatrix} k_T & \mathbf{0} \\ \mathbf{0} & \mathbf{K}_R \end{bmatrix}, \end{aligned} \quad (44)$$

where the explicit expression of $\mathbf{S}(\boldsymbol{\eta})$ is

$$\mathbf{S}(\boldsymbol{\eta}) = -\begin{bmatrix} -k_T \frac{m_d}{m} \mathbf{e}_3^T \mathbf{R}^T(\boldsymbol{\eta}) & \mathbf{0} \\ \mathbf{0} & \mathbf{K}_R \mathbf{N}^T \end{bmatrix}. \quad (45)$$

Now, similar to Section 2.4.1, and also recalling (10), the way \mathbf{u}_{di} affects the system dynamics $\dot{\mathbf{p}}$ is through $\mathbf{G}(\boldsymbol{\eta})\mathbf{u}_{di}$. It affects the *energy shaped system* dynamics $\dot{\tilde{\mathbf{p}}}$ through $\mathbf{M}_d\mathbf{M}^{-1}\mathbf{G}(\boldsymbol{\eta})\mathbf{u}_{di}$. By proceeding as in the previous section, and considering the damping injection control input computed using the noisy states, i.e., $\tilde{\mathbf{u}}_{di}$, we can write

$$\begin{aligned} \mathbf{M}_d\mathbf{M}^{-1}\mathbf{G}(\boldsymbol{\eta})\tilde{\mathbf{u}}_{di} &= \mathbf{M}_d\mathbf{M}^{-1}\mathbf{G}(\boldsymbol{\eta})\mathbf{S}(\tilde{\boldsymbol{\eta}})\dot{\tilde{\mathbf{q}}} \\ &= \mathbf{M}_d\mathbf{M}^{-1}\mathbf{G}(\boldsymbol{\eta})(\mathbf{S}(\boldsymbol{\eta})\dot{\mathbf{q}} + (\mathbf{S}(\tilde{\boldsymbol{\eta}})\dot{\tilde{\mathbf{q}}} - \mathbf{S}(\boldsymbol{\eta})\dot{\mathbf{q}})), \end{aligned} \quad (46)$$

from which we can see that the wrench generated by the state noises in the damping injection control input is

$$\mathbf{w}_{di} = \mathbf{M}_d\mathbf{M}^{-1}\mathbf{G}(\boldsymbol{\eta})(\mathbf{S}(\tilde{\boldsymbol{\eta}})\dot{\tilde{\mathbf{q}}} - \mathbf{S}(\boldsymbol{\eta})\dot{\mathbf{q}}). \quad (47)$$

After straightforward computations we can show that this wrench is in the form of

$$\mathbf{w}_{di} = -\begin{bmatrix} k_T \frac{m_d^2}{m^2} \mathbf{R}(\boldsymbol{\eta})\mathbf{e}_3^T \mathbf{R}^T(\tilde{\boldsymbol{\eta}})\dot{\tilde{\mathbf{p}}}_q - \mathbf{R}^T(\boldsymbol{\eta})\dot{\mathbf{p}}_q \\ \mathbf{N}\mathbf{K}_R\mathbf{N}^T\dot{\tilde{\boldsymbol{\eta}}}_N \end{bmatrix}. \quad (48)$$

Thus, \mathbf{w}_{di} is given by a bounded torque and by a force. Since torques are fully actuated, the torque disturbances are counter-actuated by the elastic potential and their effect is only to change the equilibrium point. Forces are more dangerous, because they may act along the underactuated directions (\mathbf{x} and \mathbf{y}). However, note that these forces vanish with a decreasing damping parameter k_T , which is as expected from any damping-based control action. In the case of high noise magnitudes that might lead to destabilizing disturbance forces, a simple straightforward (and practical) solution may be reducing the damping gain $k_T \rightarrow 0$. In this way we do not inject additional damping on the translational direction and we keep only the aerodynamic damping that is acting on all directions, i.e., the system is still cyclo-passive.

2.4.3. Wrench compensation analysis. From (27) the control input for external wrench compensation is

$$\begin{aligned} \mathbf{u}_w &= \mathbf{K}(\boldsymbol{\eta})\mathbf{w}_{ext} \\ \mathbf{K}(\boldsymbol{\eta}) &= \mathbf{G}^+(\boldsymbol{\eta})\mathbf{M}\mathbf{M}_d^{-1}(\mathbf{I} - \mathbf{M}_d\mathbf{M}^{-1}), \end{aligned} \quad (49)$$

which, as the others before, enters to the original system dynamics as $\mathbf{G}(\boldsymbol{\eta})\mathbf{u}_w$, and to the desired (target) system dynamics as $\mathbf{M}_d\mathbf{M}^{-1}\mathbf{G}(\boldsymbol{\eta})\mathbf{u}_w$.

Although we will follow the same procedure as before, note that this time there could be two means of the noise disturbance affecting the control input;⁵ either on $\boldsymbol{\eta}$ or \mathbf{w}_{ext} . With this in mind, the noisy control input $\tilde{\mathbf{u}}_w$ enters the desired system dynamics as

$$\mathbf{M}_d\mathbf{M}^{-1}\mathbf{G}(\boldsymbol{\eta})\tilde{\mathbf{u}}_w = \mathbf{M}_d\mathbf{M}^{-1}\mathbf{G}(\boldsymbol{\eta})\mathbf{K}(\tilde{\boldsymbol{\eta}})\tilde{\mathbf{w}}_{ext}, \quad (50)$$

where

$$\tilde{\mathbf{w}}_{ext} = \mathbf{w}_{ext} + \mathbf{w}_{extN} = \begin{bmatrix} \mathbf{f}_{ext} \\ \boldsymbol{\tau}_{ext} \end{bmatrix} + \begin{bmatrix} \mathbf{f}_{extN} \\ \boldsymbol{\tau}_{extN} \end{bmatrix} \quad (51)$$

indicates the noisy wrench measurement with $\mathbf{w}_{extN} \in \mathbb{R}^6$ is the bounded noise/disturbance affecting this measurement. Then, following the same procedure as in the previous section, we can find the wrench appearing due to the noises in the wrench compensating control inputs as

$$\mathbf{w}_{co} = \mathbf{M}_d\mathbf{M}^{-1}\mathbf{G}(\boldsymbol{\eta})\mathbf{K}(\tilde{\boldsymbol{\eta}})\tilde{\mathbf{w}}_{ext} - \mathbf{K}(\boldsymbol{\eta})\mathbf{w}_{ext}. \quad (52)$$

Now, let us analyze this wrench in different cases:

- noise only on \mathbf{w}_{ext}

$$\begin{aligned} \mathbf{w}_{co} &= \mathbf{M}_d\mathbf{M}^{-1}\mathbf{G}(\boldsymbol{\eta})\mathbf{K}(\boldsymbol{\eta})(\tilde{\mathbf{w}}_{ext} - \mathbf{w}_{ext}) \\ &= \begin{bmatrix} \mathbf{R}(\boldsymbol{\eta})\mathbf{e}_3\mathbf{e}_3^T\mathbf{R}^T(\boldsymbol{\eta})\mathbf{D} & \mathbf{0} \\ \mathbf{0} & (\mathbf{I} - \mathbf{N}) \end{bmatrix} \mathbf{w}_{extN} \end{aligned} \quad (53)$$

- noise only on $\boldsymbol{\eta}$

$$\begin{aligned} \mathbf{w}_{co} &= \mathbf{M}_d\mathbf{M}^{-1}\mathbf{G}(\boldsymbol{\eta})(\mathbf{K}(\tilde{\boldsymbol{\eta}}) - \mathbf{K}(\boldsymbol{\eta}))\mathbf{w}_{ext} \\ &= \begin{bmatrix} \mathbf{R}(\boldsymbol{\eta})\mathbf{e}_3\mathbf{e}_3^T(\mathbf{R}^T(\tilde{\boldsymbol{\eta}}) - \mathbf{R}^T(\boldsymbol{\eta}))\mathbf{D} & \mathbf{0} \\ \mathbf{0} & \mathbf{0} \end{bmatrix} \mathbf{w}_{ext} \end{aligned} \quad (54)$$

- noise only on both \mathbf{w}_{ext} and $\boldsymbol{\eta}$

$$\begin{aligned} \mathbf{w}_{co} &= \mathbf{M}_d\mathbf{M}^{-1}\mathbf{G}(\boldsymbol{\eta})(\mathbf{K}(\tilde{\boldsymbol{\eta}}) - \mathbf{K}(\boldsymbol{\eta}))(\tilde{\mathbf{w}}_{ext} - \mathbf{w}_{ext}) \\ &= \begin{bmatrix} \mathbf{R}(\boldsymbol{\eta})\mathbf{e}_3\mathbf{e}_3^T\mathbf{R}^T(\tilde{\boldsymbol{\eta}})\mathbf{D} & \mathbf{0} \\ \mathbf{0} & (\mathbf{I} - \mathbf{N}) \end{bmatrix} \tilde{\mathbf{w}}_{ext} \\ &\quad - \begin{bmatrix} \mathbf{R}(\boldsymbol{\eta})\mathbf{e}_3\mathbf{e}_3^T\mathbf{R}^T(\boldsymbol{\eta})\mathbf{D} & \mathbf{0} \\ \mathbf{0} & (\mathbf{I} - \mathbf{N}) \end{bmatrix} \mathbf{w}_{ext} \\ &= \begin{bmatrix} \mathbf{R}(\boldsymbol{\eta})\mathbf{e}_3\mathbf{e}_3^T(\mathbf{R}^T(\tilde{\boldsymbol{\eta}}) - \mathbf{R}^T(\boldsymbol{\eta}))\mathbf{D}\mathbf{f}_{extN} \\ (\mathbf{I} - \mathbf{N})\boldsymbol{\tau}_{extN} \end{bmatrix} \end{aligned} \quad (55)$$

where $\mathbf{D} = \mathbf{I} \frac{m-m_d}{m}$.

Note that the effect of the measurement noises on the external wrench compensating control input along the fully actuated directions (rotational) are either bounded (which can always be counteracted), or they never appear. On the other hand, the disturbing forces due to the measurement noises along the underactuated directions can be dangerous, which in each scenario can be canceled when setting $m_d = m \Rightarrow \mathbf{D} = \mathbf{0}$.

In summary, dividing the IDA-PBC control input into its components explicitly shows which part of it is more problematic in terms of robustness against the noises (or inaccuracy) on the measurements. The energy shaping input \mathbf{u}_{es} is not affected by the noises along the underactuated directions, and for the actuated directions the effect of noise is bounded. The damping injection control input is affected by the noises along the underactuated directions, which is harder to deal with (it is also affected by the noises along the actuated directions, but their effect only disturbs the system around its equilibrium, which can always be counteracted). However, by choosing $k_T \rightarrow 0$, one can avoid the wrenches caused by the noise. Similarly, the external wrench compensating control input is also affected by the noises, and it is again not trivial to compensate for the disturbing forces along the underactuated directions. One idea might be to set $m_d = m \Rightarrow \mathbf{D} = \mathbf{0}$, which removes the effects of the noises along the underactuated directions, however this would be a conservative action since in this case one cannot assign a desired mass to the quadrotor.

Note that the high-level external control input \mathbf{u}_o is still free to use for dealing with the effects of the measurement noises, which is a potential field of study in the scope of our future works.

Remark 2. Here we presented a robustness analysis of the control input \mathbf{u}_i against the noisy state and wrench measurements. To this end, note that both the controller

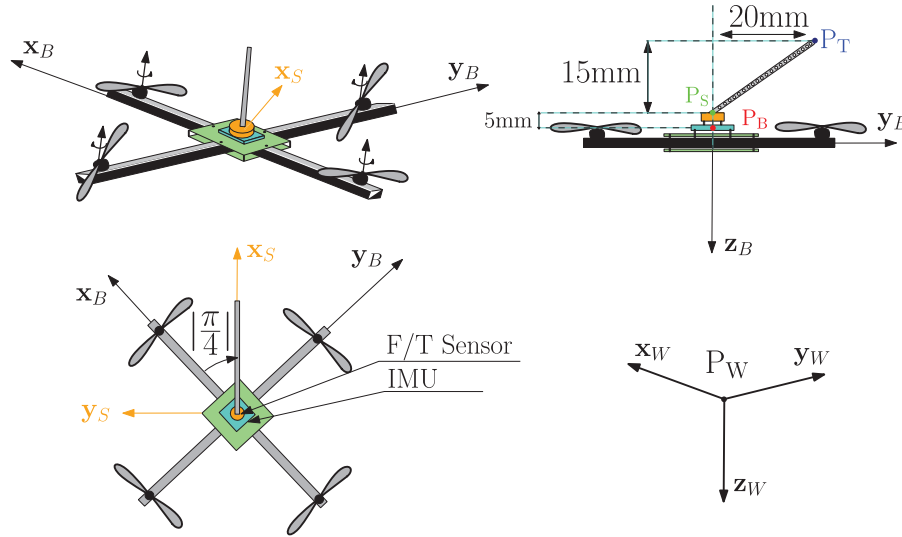


Fig. 3. Placement of the interaction tool tip on top of the quadrotor: IMU (turquoise), F/T sensor (orange), and the rigid tool (gray) and its tip (blue). This setup is later realized both as a CAD model and in reality as shown in Figure 4. The distances shown here match with the real design.

presented in Section 2.3 and the external wrench estimation (to be presented in Section 3.1) are done for the CoM of the system, namely the dynamics representing the motion of point P_B , that is the center of the quadrotor body-fixed frame. Although the physical interaction considered in this paper is always through an interaction tool (see Figure 3), its impact on the CoM dynamics is a matter of kinematics (with negligible tool mass) and subject to the rigid-body transformations, as also studied in Section 3.2.

Remark 3. We note that quantitative analysis on the robustness of the proposed controller to parametric uncertainties (e.g., mass, moment of inertia) is in the scope of our future works. Moreover, considering the dynamics of the interaction tool and controlling the tool-tip dynamics instead of the CoM of the quadrotor is another direction that extends the results of this paper.

3. External wrench: estimation versus measurement

To achieve meaningful control of APhI, knowledge of the external wrench is essential. Here we discuss two methods: indirect (estimation) and direct (measurement). Each method can overcome the other for different reasons. By estimating the external wrench, one can avoid additional hardware cost and weight (and, thus, increase the duration of flight). In particular, for miniature VTOL quadrotors, the load capacity is quite limited and they are not suited for carrying a heavy F/T transducer and its electronics. Moreover, an estimator can be developed for any point on the flying robot, whereas the information provided by the transducer is limited to its location,⁶

On the other hand, F/T sensors provide typically more reliable measurements which are not affected by any

modeling or estimation error. While an estimator must rely on the measurements of the other sensors, e.g., camera or IMU, F/T sensors give accurate and independent measurements. In particular, for outdoor implementations of the quadrotors, using F/T sensors can be indispensable, because the state estimation is already a challenging problem in outdoor environments.

In this section, we describe the external wrench estimator proposed in Yüksel et al. (2014a). Then we provide a measurement method using a low-cost lightweight 6D F/T sensor placed onboard of a quadrotor. Finally, we compare the results of these two methods in an experimental scenario, and promote the use of the F/T sensors for APhI tasks.

3.1. External wrench estimation

Wrench estimation for flying robots has been studied by different robotics groups. In Augugliaro and D’Andrea (2013) a *Kalman filter* is used to estimate the external force. A more general method was proposed in Ruggiero et al. (2014), where a residual *momentum-based* wrench estimator for quadrotors is presented. This method was further analyzed by Tomic and Haddadin (2014). In McKinnon and Schoellig (2016) an algorithm based on *unscented quaternion estimator* was used for estimating the external wrenches acting on a quadrotor body.

In Yüksel et al. (2014a) we presented a *nonlinear Lyapunov-based* disturbance observer for estimating the external wrenches acting on a quadrotor. For that, we have considered the Lagrange dynamics of the system as

$$\mathbf{w}_{ext} = \mathbf{B}(\mathbf{q})\ddot{\mathbf{q}} + \mathbf{C}(\mathbf{q}, \dot{\mathbf{q}})\dot{\mathbf{q}} + \mathbf{g} - \mathbf{G}(\mathbf{q})\mathbf{u}, \quad (56)$$

with

$$\begin{aligned} \mathbf{B}(\mathbf{q}) &= \begin{bmatrix} m\mathbf{I} & * \\ \mathbf{0} & {}^W\mathbf{M}_{qr}(\boldsymbol{\eta}) \end{bmatrix} = \mathbf{B}^T \in \mathbb{R}^{6 \times 6}, \\ \mathbf{G}(\mathbf{q}) &= \begin{bmatrix} -\mathbf{R}(\boldsymbol{\eta})\mathbf{e}_3 & \mathbf{0} \\ \mathbf{0} & \mathbf{I} \end{bmatrix} \in \mathbb{R}^{6 \times 4} \\ \mathbf{C}(\mathbf{q}, \dot{\mathbf{q}}) &= \begin{bmatrix} \mathbf{0} & \mathbf{0} \\ \mathbf{0} & \mathbf{C}_r(\boldsymbol{\eta}, \dot{\boldsymbol{\eta}}) \end{bmatrix} \in \mathbb{R}^{6 \times 6}, \quad \mathbf{g} = \begin{bmatrix} -mg\mathbf{e}_3 \\ \mathbf{0} \end{bmatrix}, \end{aligned} \quad (57)$$

where ${}^W\mathbf{M}_{qr}(\boldsymbol{\eta}) = \mathbf{T}(\boldsymbol{\eta})^T \mathbf{M}_{qr} \mathbf{T}(\boldsymbol{\eta}) \in \mathbb{R}^{3 \times 3}$ is the rotational inertia matrix with respect to \mathcal{F}_W and $\mathbf{C}_r(\boldsymbol{\eta}, \dot{\boldsymbol{\eta}}) \in \mathbb{R}^{3 \times 3}$ is the matrix representing the Coriolis terms for the rotational dynamics. See more details in Yüksel et al. (2014a) and Yüksel (2017).

It has been shown in Chen et al. (2000) and Nikoobin and Haghghi (2009) that for a similar model (serial manipulator arm), the following disturbance observer can be proposed

$$\begin{aligned} \dot{\hat{\mathbf{w}}}_{ext} &= \mathbf{L}(\mathbf{q}, \dot{\mathbf{q}})(\mathbf{w}_{ext} - \hat{\mathbf{w}}_{ext}) \\ &= -\mathbf{L}(\mathbf{q}, \dot{\mathbf{q}})\hat{\mathbf{w}}_{ext} + \mathbf{L}(\mathbf{q}, \dot{\mathbf{q}})(\mathbf{B}(\mathbf{q})\ddot{\mathbf{q}} + \mathbf{C}(\mathbf{q}, \dot{\mathbf{q}})\dot{\mathbf{q}} \\ &\quad + \mathbf{g} - \mathbf{G}(\mathbf{q})\mathbf{u}), \end{aligned} \quad (58)$$

where $\hat{\mathbf{w}}_{ext} = [\hat{\mathbf{f}}_{ext}^T \hat{\boldsymbol{\tau}}_{ext}^T]^T \in \mathbb{R}^6$ is the estimated wrench and $\mathbf{L}(\mathbf{q}, \dot{\mathbf{q}}) \in \mathbb{R}^{6 \times 6}$ will be designed in order to ensure the convergence of the observer. Note that we do not have any specific model of the external disturbance, hence we assume $\dot{\mathbf{w}}_{ext} = \mathbf{0}$. Then the observer error and its dynamics are

$$\begin{aligned} \mathbf{e}_o &= \mathbf{w}_{ext} - \hat{\mathbf{w}}_{ext} \\ \dot{\mathbf{e}}_o &= \dot{\mathbf{w}}_{ext} - \dot{\hat{\mathbf{w}}}_{ext} = \mathbf{L}(\mathbf{q}, \dot{\mathbf{q}})\hat{\mathbf{w}}_{ext} - \mathbf{L}(\mathbf{q}, \dot{\mathbf{q}})\mathbf{w}_{ext}, \end{aligned} \quad (59)$$

which can be expressed as

$$\dot{\mathbf{e}}_o + \mathbf{L}(\mathbf{q}_q, \dot{\mathbf{q}}_q)\mathbf{e}_o = \mathbf{0}. \quad (60)$$

This means that the choice of $\mathbf{L}(\mathbf{q}, \dot{\mathbf{q}})$ will directly affect the asymptotic stability of the error dynamics.

Note that in order to implement (58) one needs knowledge of $\dot{\mathbf{q}}$, $\ddot{\mathbf{q}}$, and $\ddot{\mathbf{q}}$, where for many platforms acceleration measurements might not be reliable or not even available (e.g., for quadrotors the angular accelerations are not available for the common platforms). For this purpose, we define the auxiliary vector:

$$\boldsymbol{\Psi} = \hat{\mathbf{w}}_{ext} - \boldsymbol{\gamma}(\dot{\mathbf{q}}). \quad (61)$$

Now, by taking the time derivative of (61) and equating it to (58), and choosing

$$\frac{\partial \boldsymbol{\gamma}(\dot{\mathbf{q}})}{\partial \dot{\mathbf{q}}} = \mathbf{L}(\mathbf{q}, \dot{\mathbf{q}})\mathbf{B}(\mathbf{q}), \quad (62)$$

we can find the dynamics of the nonlinear observer as

$$\begin{aligned} \dot{\boldsymbol{\Psi}} &= -\mathbf{L}(\mathbf{q}, \dot{\mathbf{q}})\boldsymbol{\Psi} \\ &\quad + \mathbf{L}(\mathbf{q}, \dot{\mathbf{q}})(\mathbf{C}(\mathbf{q}, \dot{\mathbf{q}})\dot{\mathbf{q}} + \mathbf{g} - \mathbf{G}(\mathbf{q})\mathbf{u} - \boldsymbol{\gamma}(\dot{\mathbf{q}})) \\ \dot{\hat{\mathbf{w}}}_{ext} &= \boldsymbol{\Psi} + \boldsymbol{\gamma}(\dot{\mathbf{q}}). \end{aligned} \quad (63)$$

As can be seen from (60), we must choose $\mathbf{L}(\mathbf{q}, \dot{\mathbf{q}})$ in such a way that the error dynamics become asymptotically stable. Moreover, the decision made in (62) brings a strict dependency of $\mathbf{L}(\mathbf{q}, \dot{\mathbf{q}})$ on the choice of $\boldsymbol{\gamma}(\dot{\mathbf{q}})$. We make the following choice:

$$\begin{aligned} \boldsymbol{\gamma}(\dot{\mathbf{q}}_q) &= c_o \dot{\mathbf{q}}_q \\ \mathbf{L}(\mathbf{q}, \dot{\mathbf{q}}) &= c_o \mathbf{B}(\mathbf{q})^{-1}, \end{aligned} \quad (64)$$

for $c_o > 0$ is the observer gain.

Proposition 3. Consider the wrench estimator (63) and assume that the roll and pitch velocities are bounded, i.e., $|\dot{\phi}| < \bar{\phi}$ and $|\dot{\theta}| < \bar{\theta}$, where $\bar{\phi}, \bar{\theta} \in \mathbb{R}^+$. If $\dot{\mathbf{w}}_{ext} = \mathbf{0}$ holds and if $\mathbf{L}(\mathbf{q}, \dot{\mathbf{q}})$ is defined as in (64), then it is possible to have $\hat{\mathbf{w}}_{ext} \rightarrow \mathbf{w}_{ext}$.

Proof. We provide a sketch of the proof here; more details can be found in Yüksel et al. (2014a). To do so, we will show that the estimation error defined in (59) will asymptotically vanish because the error dynamics (60) is asymptotically stable at $\mathbf{e} = \mathbf{0}$. Let

$$V(\mathbf{e}_o, \mathbf{q}) = \mathbf{e}_o^T \mathbf{B}(\mathbf{q})\mathbf{e}_o \quad (65)$$

be a positive-definite candidate Lyapunov function. Considering (60) and (62), we can write

$$\begin{aligned} \dot{V} &= 2\mathbf{e}_o^T \dot{\mathbf{B}}\mathbf{e}_o + \mathbf{e}_o^T \ddot{\mathbf{B}}\mathbf{e}_o = -2\mathbf{e}_o^T \mathbf{B}\mathbf{L}\mathbf{e}_o + \mathbf{e}_o^T \ddot{\mathbf{B}}\mathbf{e}_o \\ &= -2c_o \mathbf{e}_o^T \mathbf{e}_o + \mathbf{e}_o^T \ddot{\mathbf{B}}\mathbf{e}_o. \end{aligned} \quad (66)$$

The first component of the right-hand side of (66) is negative definite for $c_o \in \mathbb{R}^+$. The second component has an indefinite sign. Nevertheless, because $\mathbf{B}(\mathbf{q}) = \mathbf{B}^T(\mathbf{q})$, $\dot{\mathbf{B}}(\mathbf{q}, \dot{\mathbf{q}})$ is symmetric and, therefore, its eigenvalues are real. As $|\dot{\phi}| < \bar{\phi}$ and $|\dot{\theta}| < \bar{\theta}$, from Yüksel et al. (2014a) and Yüksel (2017), it is easy to find two finite numbers $\alpha, \beta \in \mathbb{R}$ such that $\alpha < \dot{B}_{ij} < \beta$, $i, j \in \{1, \dots, 6\}$, where \dot{B}_{ij} is the ij th element of $\dot{\mathbf{B}}$. Thus, as shown in Zhan (2006), it is always possible to find a finite upper bound λ_B for all the possible eigenvalues of $\dot{\mathbf{B}}(\mathbf{q}_q, \dot{\mathbf{q}}_q)$:

$$\max_{\mathbf{q}, \dot{\mathbf{q}}} \lambda_M \{ \dot{\mathbf{B}}(\mathbf{q}, \dot{\mathbf{q}}) \} \leq \lambda_B < \infty, \quad (67)$$

where $\lambda_M \{ \dot{\mathbf{B}}(\mathbf{q}, \dot{\mathbf{q}}) \}$ is the maximum eigenvalue of $\dot{\mathbf{B}}(\mathbf{q}, \dot{\mathbf{q}})$. Thus, we have that

$$\mathbf{e}_o^T \dot{\mathbf{B}}\mathbf{e}_o \leq \lambda_B \mathbf{e}_o^T \mathbf{e}_o. \quad (68)$$

It is therefore possible to choose a $c_o > \frac{\lambda_B}{2}$ that implies \dot{V} is negative definite and that, therefore, $\mathbf{e}_o(t) \rightarrow \mathbf{0}$, which proves the statement. ■

3.2. External wrench measurement

Measuring contact forces and torques is possible using F/T sensors, which are already in use for robotic manipulators and humanoids (see Siciliano and Khatib, 2008). Recently,

they have been in use also in aerial robots. In Gioioso et al. (2014), it was shown how a quadrotor can be turned into a 3D force tool, and for the experimental setup an F/T sensor was used. In that work, like many others, the F/T sensor is either placed in the environment, e.g., mounted on a wall, or on the robot but only when it is not completely flying, i.e., when the robot is fixed to a test bench as in Yu and Ding (2012) and Schiano et al. (2014). One of the main reasons why these sensors are not yet used on board of a flying aerial vehicle is because of their weight. In particular, considering their electronics, e.g., the data acquisition box, most of the aerial robots used in research projects are not capable of flying with these sensors on board.

However, recently some lightweight 6D F/T sensors appeared on the market. For the experiments of this paper, we have decided to use the *FTSens* 6D F/T sensor, developed by the *Italian Institute of Technology* (IIT), as introduced in Fumagalli et al. (2012a). This sensor weights 0.122 [kg] including all the electronics and its costs is relatively low w.r.t its pairs in the market. All these factors make this sensor a suitable candidate to be used on board of an aerial robot. This paves the way of using them as direct measurement sources, which feed the wrench measurements back to the control algorithms (e.g., the one sketched in Figure 2). The details of the hardware and software for the *FTSens* F/T sensor is given in Section 4.2, and the experimental setup consisting of a quadrotor equipped with this sensor is shown in Figure 4. To our best knowledge, this is the first quadrotor setup in the literature, which can freely fly with a 6D F/T sensor and its all electronics onboard, and perform APhI tasks.

Now let us give the details of its usage on board of a quadrotor VTOL. A sketch of our quadrotor and the F/T sensor setup is given in Figure 3. On top of the F/T sensor a rigid tool is placed, intended to be used as the *interaction* tool with the environment (note that the mass of the manipulation tool is part of the overall quadrotor mass, but it is not considered separately for the controller.). We intentionally placed this rigid tool in a way, that there is $|\pi/4|$ [rad] between the tool tip and the quadrotor frame; so that the propellers will be away from the obstacles when the tooltip is interacting with its environment. The CAD design of this setup is shown in Figure 4, where we also present its realization in detail.

Unlike a model-based indirect estimation method, e.g., that presented in Section 3.1, with using transducers our measurements are limited to the location of the sensor. Hence, now our goal is to compute the external wrenches acting on different parts of the quadrotor, using the measurements acquired from the F/T sensor and rigid-body coordinate transformation methods. We had previously defined $\mathcal{F}_W : \{\mathbf{P}_W, \mathbf{x}_W, \mathbf{y}_W, \mathbf{z}_W\}$ as the world frame, and $\mathcal{F}_B : \{\mathbf{P}_B, \mathbf{x}_B, \mathbf{y}_B, \mathbf{z}_B\}$ as the body-fixed frame of the quadrotor. Now, let us define $\mathcal{F}_S : \{\mathbf{P}_S, \mathbf{x}_S, \mathbf{y}_S, \mathbf{z}_S\}$ as the F/T sensor frame. Assume that the inertial measurement unit (IMU) frame is the same as \mathcal{F}_B . Then define $\mathcal{F}_{Sb} : \{\mathbf{P}_S, \mathbf{x}_{Sb}, \mathbf{y}_{Sb}, \mathbf{z}_{Sb}\}$ as the frame of the F/T sensor,

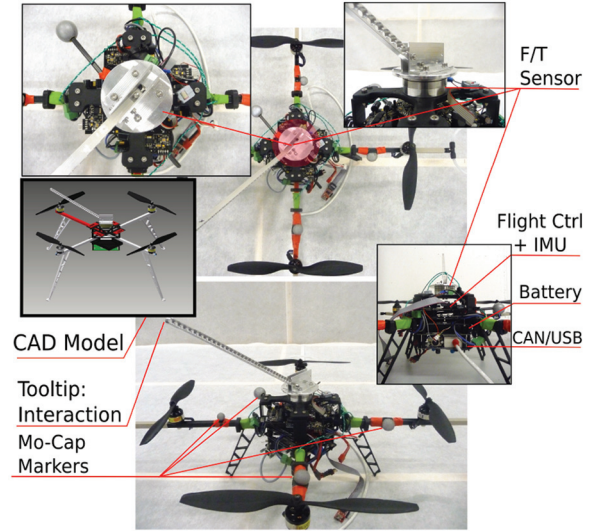


Fig. 4. Quadrotor with F/T sensor (*FTSens*) on board. This is the experimental setup. Note that the CAD model is developed based on the description in Figure 3, and so is the real robot. Both the F/T sensor and the interaction tool are placed on top of the quadrotor. The hardware for the CAN–USB communication, is placed on the bottom of the robot. For this setup, $m = 1.49\text{kg}$, and $\mathbf{M}_{qr} = \text{diag}([0.01708, 0.0172, 0.0274]) \in \mathbb{R}^{3 \times 3}$ in units of kgm^2 .

after its orientation is aligned with the orientation of the body-fixed frame. Then let us define the following wrench information.

- The external wrench acting at and about the tip point of the tool (\mathbf{P}_T) is defined with $\mathbf{w}_t \in \mathbb{R}^6$ in \mathcal{F}_W , because the external forces and torques are coming from the world frame.
- The wrench measured by the sensor is defined with $\tilde{\mathbf{w}}_s \in \mathbb{R}^6$ in \mathcal{F}_S , because the measurements are taken in the sensor frame.
- The wrench measured by the sensor and adapted to the body frame is defined with $\mathbf{w}_s \in \mathbb{R}^6$ in \mathcal{F}_{Sb} , because the sensor is fixed to the body of the quadrotor.
- The wrench entering the quadrotor dynamics is defined with $\mathbf{w}_{ext} \in \mathbb{R}^6$, where the forces are defined in \mathcal{F}_W and the torques are in \mathcal{F}_B so equivalently in \mathcal{F}_{Sb} . This is because of the choice made when writing the quadrotor equations of motion in Section 2.3, where the translational dynamics is written in the world frame, whereas the rotational dynamics is in the body frame. Note also that the controller developed in this paper accepts this wrench as an input (see also Figure 2).

Now, it is clear that the only measurement we get is $\tilde{\mathbf{w}}_s \in \mathbb{R}^6$ in \mathcal{F}_S , but we need $\mathbf{w}_{ext} \in \mathbb{R}^6$ for the controller presented in Section 2.3, and maybe also $\mathbf{w}_t \in \mathbb{R}^6$ in \mathcal{F}_W for visualization or for another type of controller. Then let

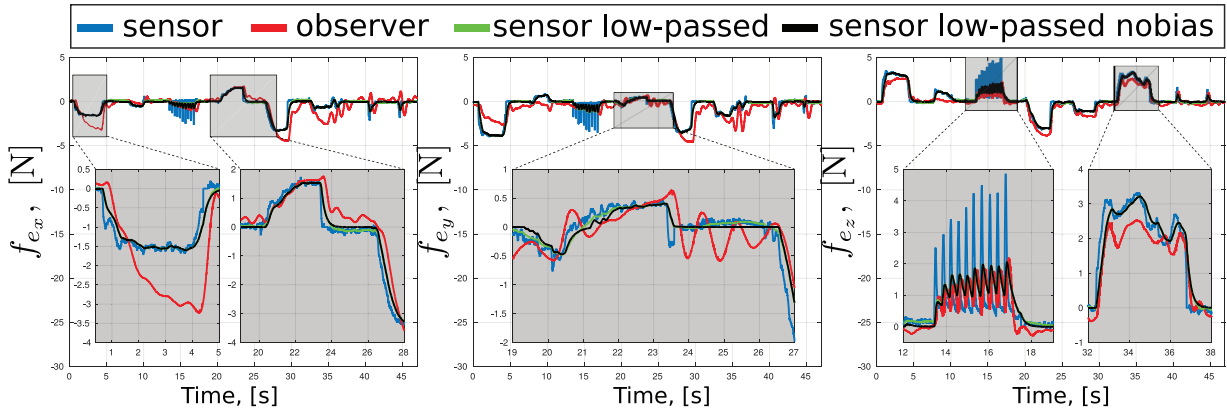


Fig. 5. Comparison between the F/T sensor (see Section 3.2) and the observer (see Section 3.1). Only the measured/estimated forces are shown, in units of Newtons. Raw sensor readings are depicted with blue curves, and the output of the observer is depicted with red curves. Green is used for the measured forces that are *low-pass filtered*. Black curves are used when the bias of this low-pass filtered data is removed in real time (which we used in our experiments in Section 4 when implementing the IDA-PBC method, with also considering the transformations explained in Section 3.2). The magnified plots of each grayed box are placed close by for better comparison of the different values.

us clarify the following relationship between the different wrench information.

- Find $\mathbf{w}_s \in \mathbb{R}^6$ in \mathcal{F}_{Sb} . To do so, change the F/T sensor frame from \mathcal{F}_S to \mathcal{F}_{Sb} . Note that it can be done using time invariant rotations only (see Figure 3 for the orientations of the frames). More specifically, remembering that $\mathcal{F}_S : \{\mathbf{P}_S, \mathbf{x}_S, \mathbf{y}_S, \mathbf{z}_S\}$ and $\mathcal{F}_{Sb} : \{\mathbf{P}_S, \mathbf{x}_{Sb}, \mathbf{y}_{Sb}, \mathbf{z}_{Sb}\}$, we have

$$\begin{bmatrix} \mathbf{x}_{Sb} \\ \mathbf{y}_{Sb} \\ \mathbf{z}_{Sb} \end{bmatrix} = \mathbf{R}_S^B \begin{bmatrix} \mathbf{x}_S \\ \mathbf{y}_S \\ \mathbf{z}_S \end{bmatrix}, \quad \mathbf{R}_S^B = \mathbf{R}_{x_S}(\pi) \mathbf{R}_{z_S}(\pi/4), \quad (69)$$

where \mathbf{R}_{*S} is the rotation matrix defined in \mathcal{F}_S and around the $*$ -axis. Hence, if $\tilde{\mathbf{w}}_s \in \mathbb{R}^6$ is the measurement of the F/T sensor defined in \mathcal{F}_S (because it is fixed in the sensor frame), then

$$\mathbf{w}_s = \begin{bmatrix} \mathbf{R}_S^B & \mathbf{0} \\ \mathbf{0} & \mathbf{R}_S^B \end{bmatrix} \tilde{\mathbf{w}}_s \quad (70)$$

is the measurement but defined⁷ in \mathcal{F}_{Sb} . Note that \mathbf{R}_S^B is a constant (time invariant) matrix, and $\mathbf{0}$ is a matrix that consists of only zeros.

- Find $\mathbf{w}_t \in \mathbb{R}^6$ in \mathcal{F}_W . To do so, let us use the recently computed \mathbf{w}_s . This can be done using the following relation:

$$\mathbf{w}_s = \begin{bmatrix} \mathbf{R}_W^B(\boldsymbol{\eta}) & \mathbf{0} \\ [\mathbf{d}_l] \mathbf{R}_W^B(\boldsymbol{\eta}) & \mathbf{R}_W^B(\boldsymbol{\eta}) \end{bmatrix} \mathbf{w}_t, \quad (71)$$

where $\mathbf{R}_W^B(\boldsymbol{\eta})$ is the rotation matrix representing the orientation of \mathcal{F}_W in \mathcal{F}_B , which is time variant owing to the

dependency of the quadrotor orientation $\boldsymbol{\eta} \in \mathbb{R}^3$. Note that $\mathbf{d}_l \in \mathbb{R}^3$ is the distance between \mathbf{P}_T and \mathbf{P}_S in \mathcal{F}_{Sb} frame,⁸ and $[\star]_{\wedge} : \mathbb{R}^3 \rightarrow \text{so}(3)$ is the skew-symmetric operator. Hence, using \mathbf{w}_s from (70), we can compute \mathbf{w}_t using the relation in (71).

- Find $\mathbf{w}_{ext} \in \mathbb{R}^6$. To do so, use the rigid transformation from \mathbf{w}_s to \mathbf{w}_{ext} :

$$\mathbf{w}_{ext} = \begin{bmatrix} \mathbf{R}_B^W(\boldsymbol{\eta}) & \mathbf{0} \\ [\mathbf{d}_s] \mathbf{R}_B^W(\boldsymbol{\eta}) & \mathbf{I} \end{bmatrix} \mathbf{w}_s, \quad (72)$$

where $\mathbf{R}_B^W(\boldsymbol{\eta})$ is the rotation matrix representing the orientation of \mathcal{F}_B in \mathcal{F}_W , \mathbf{I} is an identity matrix, and \mathbf{d}_s is the distance between \mathbf{P}_S and \mathbf{P}_B in \mathcal{F}_B , which is $\mathbf{d}_s = [0 \ 0 \ -0.05]$ m.

Hence, for finding the effect of \mathbf{w}_t (defined in \mathcal{F}_W) to the body-fixed frame of the quadrotor (this effect is named as \mathbf{w}_{ext} in our convention), one can first use the F/T sensor measurements $\tilde{\mathbf{w}}_s$ in \mathcal{F}_S , then compute \mathbf{w}_s in \mathcal{F}_{Sb} , and then finally use (72). For finding what \mathbf{w}_t exactly is, one can use (71).

Note that when using the North, East, Down (NED) convention, the rotation matrix from body to the world frame is $\mathbf{R}_B^W(\boldsymbol{\eta}) = \mathbf{R}$ where $\mathbf{R} \in \text{SO}(3)$ as mentioned in Section 2.3 and it is true that $\mathbf{R}_W^B(\boldsymbol{\eta}) = \mathbf{R}_B^{W^T}(\boldsymbol{\eta})$.

3.3. Comparison between estimation and direct measurement

In Yüksel et al. (2014a) the numerical (simulative) results of the wrench estimation (Section 3.1) have been presented. There, decent wrench estimation performances have been achieved, even when the noises of the other measurements are taken into account. The performance of the proposed

observer strongly relies on the choice of the observer gain (see Yüksel et al., 2014a).

Although tuning this gain in the numerical simulations was relatively easy, for the real experiments it was difficult to find a compromise between the convergence of the estimation and its performance, as will be shown in the following comparison.

For the experimental setup, we used the aerial robot in Figure 4, where the overall quadrotor is controlled using the IDA-PBC controller (explained in Section 2.3). We then implemented the nonlinear wrench observer (given in Section 3.1). For the experiment we have disturbed the hovering quadrotor by changing external forces and torques at the tip point of the rigid link (see Figure 4), which is rigidly attached to the F/T sensor that is placed on board of the quadrotor (more details of the experimental setup are given in Section 4).

The online collected external force data are presented in Figure 5, where the F/T sensor measurements (see the sensor details in Section 4.2) are compared with the wrench observer values.⁹ The blue curves show the raw sensor measurements and the green curves are low-pass filtered versions of the blue ones. Further fine-tuning is done by removing the sensor bias online and the result is depicted with black curves. The observer data are shown in red. As can be seen from Figure 5, the observer follows the sensor data (which one may consider also as the ground truth), but with some oscillations and even with some offset. This is mainly due to the poor tuning of the observer gain c_o , and partly due to the small imprecision of the mathematical model. In particular for f_{e_x} and f_{e_y} , the observer performs worse than the sensor data. However, note that for f_{e_z} , the observer tracks the sensor data much better, because it is the direction where the aerial platform is fully actuated. Note that although the model errors, e.g., imprecise mass of the system still causes some offsets, the overall estimation is less oscillatory compared with f_{e_x} and f_{e_y} .

We also note that different estimation methods, e.g., that in [McKinnon and Schoellig (2016)], might perform better under certain conditions. However, it is noticeable that using an F/T sensor allows the exact wrench information to be acquired, independent from any system model. Moreover, in this case the wrench information would not be corrupted by any other sensor measurement, e.g., those that provide the state of the robot (see “IMU” and “MoCap” in Section 4.1). There could be a case in which the state of the robot might be miscalculated, which might not be crucial when the robot is in *free flight*, i.e., not in APhI, but in the case of APhI this might bring instability if the wrench estimation is used in the controller. Such a case can occur more frequently, especially when the robot is performing an outdoor task, where accurate state estimation of the flying robot is already a major challenge considering different weather, light, and environmental conditions.

Consequently, using a low-cost, lightweight F/T sensor could be a beneficial choice, providing robust and accurate measurements for the indoor and future outdoor

experiments. For all these reasons, we chose to use the F/T sensor setup for our APhI experiments in this paper.

4. Experiments

The experiments are managed using a stationary PC with Linux 14.04 on it, which communicates with the experimental setup (robot in Figure 4) through serial channels. In addition to the codes embedded on board of the quadrotor setup, all experiments are programmed in this PC in ROS-Indigo environment and *TeleKyb* framework: an open-source end-to-end ROS-based software for general-purpose mobile robot control developed at Max Planck Institute for Biological Cybernetics, Tübingen (for details, see Grabe et al., 2013). High-level decisions, e.g., hovering, trajectory assigning, or landing, are indicated to the robot using a custom joystick.

The experimental setup consists of a quadrotor equipped with various sensors including an F/T sensor on board. This sensor is connected to a rigid interaction tool (see Figure 4). We describe the individual parts of this setup in the following.

4.1. Quadrotor

The main body of the quadrotor setup is manufactured by HiSystems GmbH, and named as a *Mikrokopter* Quadrotor.¹⁰ The overall setup (including the F/T sensor and its electronics) weighs 1.49kg and from its CAD model we computed its moment of inertia as $\mathbf{M}_{qr} = \text{diag}([0.01708, 0.0172, 0.0274]) \in \mathbb{R}^{3 \times 3}$ in units of kgm^2 .

The quadrotor has four rigid bars, connecting four brushless motors (referred to as BL-Motors or BLDC) and their propellers to the main body of the robot (see Figure 4). Note that propellers are rigidly attached to their motors, as well as the motors to the bars, and bars to the body. On top of them there are four brushless motor controllers (BL-CTRL), a flight controller with an IMU on it and markers for a *motion capture* (MoCap) system, in this order. Below the rigid bars there is a battery as the energy source.

Each BL-CTRL has one ATMEGA168 μ -controller,¹¹ which is connected via I²C bus to a *flight controller* including an IMU. All brushless motors, hence propeller velocities, depicted with Ω_i in Figure 1, are controlled using a *motor controller* developed at LAAS-CNRS¹² (see also Franchi and Mallet, 2017). Through a serial channel we communicate with the flight controller, allowing us to read/write data from/to both the flight controller and the brushless motor controllers.

For state estimation of the robot, we use an external MoCap system (with six near-infrared cameras) and an IMU on board of the quadrotor. The MoCap system provides the pose of the quadrotor, $\mathbf{q} = [\mathbf{p}_q^T, \boldsymbol{\eta}^T]^T \in \mathbb{R}^6$ in the world frame at 120Hz, whereas the IMU is giving the linear acceleration, $\ddot{\mathbf{p}}_q \in \mathbb{R}^3$, in the world frame and the

angular velocity of the body (in the body frame), $\boldsymbol{\omega} \in \mathbb{R}^3$, both at 1kHz. However, for the controller in Section 2.3 and the wrench estimator in Section 3.1 we need the state of the quadrotor, i.e., \mathbf{q} and $\dot{\mathbf{q}}$, which is computed using an *unscented Kalman filter* (UKF) developed at LAAS-CNRS.¹⁵ This algorithm fuses both IMU and MoCap data and provides an estimate of the quadrotor state at 1kHz.

4.2. F/T sensor

In our experiments we used the *FTSens* F/T sensor, produced by the Italian Institute of Technology (IIT) originally for the ICub humanoid robots (see Fumagalli et al., 2012a). There are two reasons why we chose this sensor: first, it was relatively cheaper than its peers in the market; and, second, it only weights 0.122kg together with its electronics. This is definitely in the load range of our quadrotor. The sensor is provided with proper calibrations by IIT for the measurement range of interest. A challenge of using this sensor was implementing the software for acquiring the meaningful F/T measurements, from scratch. The FTSens communicates through the *controller area network* (CAN) bus channel, in which it receives the commands and sends the sensor data based on the CAN protocol.

For this setup to work, both the computer and the sensor need to be programmed properly. The software package we have created for this sensor is available for the public use.¹⁴ There we provide a description and the source codes for:

- setting up your computer (for both Intel or ARM processors) for using the CAN–USB converter;
- getting the calibration data from the sensor and letting it send the raw data to the computer.

The details on the communication protocol of the sensor are available in the wiki-page of the ICub.¹⁵ Using this *driver* it is possible to receive the *raw data* from the FTSens F/T sensor.

For processing this raw data, we implemented a ROS (C++)-based software within the TeleKyb framework.¹⁶ This software is tested with ROS-Indigo in Ubuntu 14.04 OS. It receives the raw data from the serial channel the sensor is connected to (through a CAN–USB converter) and as output returns the force and torque measurements in meaningful units as a ROS message. In this way the output can also be used by other ROS-based packages, e.g., the controller tested in Sections 4.4 and 4.5. Note that this code is strongly depended on both ROS and TeleKyb message types and their existing packages. Its usage¹⁷ for our experiments is also made available to the public,¹⁷ but for the initial access a permission from Max Planck Society would be needed.

4.3. Position tracker

A high-level position tracker is used for steering the VTOL quadrotor to a desired trajectory, while letting IDA-PBC

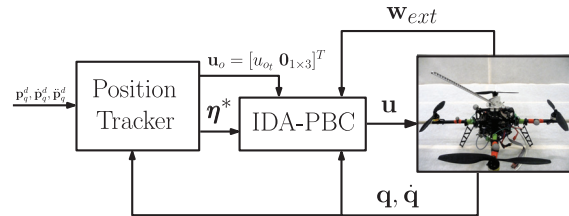


Fig. 6. Sketch of the control framework used for the experiments. The position tracker is developed based on a position controller, sending the desired attitude equilibrium $\boldsymbol{\eta}^*$ and the high-level control input \mathbf{u}_o to the IDA-PBC controller.

shape its physical properties. This tracking controller is developed based on a *position controller*, as presented in Lee et al. (2013). From the decoupling property of the quadrotor, the rotational dynamics in (7) can be computed independently from the translational dynamics given in (6). Let us consider a desired position trajectory of the quadrotor as $\mathbf{p}_q^d = [x_q^d \ y_q^d \ z_q^d]^T \in \mathbb{R}^3$, and assume that $\mathbf{f}_{ext} = \mathbf{0}$. Then, following from Lee et al. (2013), and from the third row of (6), the thrust input

$$u_{o_i} = -\frac{m_d}{c_\phi c_\theta} (\mathbf{g} + \ddot{z}_q^d + k_{d_z}(\dot{z}_q^d - \dot{z}_q) + k_{p_z}(z_q^d - z_q)) \quad (73)$$

ensures the local exponential stability of $(z_q^d - z)$, as long as $c_\phi c_\theta \neq 0$, which is violated only when the quadrotor configuration is in a singularity that we avoid all the time. The control gains $k_{d_*} \in \mathbb{R}_{\geq 0}$ and $k_{p_*} \in \mathbb{R}_{\geq 0}$ are used for removing the velocity and position errors along the $*$ -axes, respectively, where $*$ = $\{\mathbf{x}, \mathbf{y}, \mathbf{z}\}$. From the first two rows of (6) we have

$$m_d \begin{bmatrix} \ddot{x}_q \\ \ddot{y}_q \end{bmatrix} = -u_{o_i} \underbrace{\begin{bmatrix} c_\phi c_\psi & s_\psi \\ c_\phi s_\psi & -c_\psi \end{bmatrix}}_{=: \mathbf{W}(\phi, \psi) \in \mathbb{R}^{2 \times 2}} \begin{bmatrix} s_\theta \\ s_\phi \end{bmatrix}, \quad (74)$$

where \mathbf{W} is always invertible as long as $c_\phi \neq 0$, which means that the system is not in singularity. Then choosing the following roll and pitch commands will make $(x_q^d - x_q, y_q^d - y_q)$ locally exponentially stable

$$\begin{bmatrix} \bar{\theta}_c = s_{\phi^d} \\ \bar{\phi}_c = s_{\psi^d} \end{bmatrix} = -\frac{m_d \mathbf{W}^{-1}}{u_{o_i}} \begin{bmatrix} \ddot{x}_q^d + k_{d_x}(\dot{x}_q^d - \dot{x}_q) + k_{p_x}(x_q^d - x_q) \\ \ddot{y}_q^d + k_{d_y}(\dot{y}_q^d - \dot{y}_q) + k_{p_y}(y_q^d - y_q) \end{bmatrix}. \quad (75)$$

In this step of the computations, let us define some maximum boundaries to both roll and pitch commands, preventing the system coming close to its singularities. In our experiments, we choose $\phi_c^{max} = \theta_c^{max} = \sin(r_l)$, where $r_l = 0.52326$ rad. Then let us implement the following soft saturation for both roll and pitch commands:

$$\phi_c = \frac{2\phi_c^{max}}{\pi} \arctan\left(\frac{\bar{\phi}_c}{2\phi_c^{max}}\right)$$

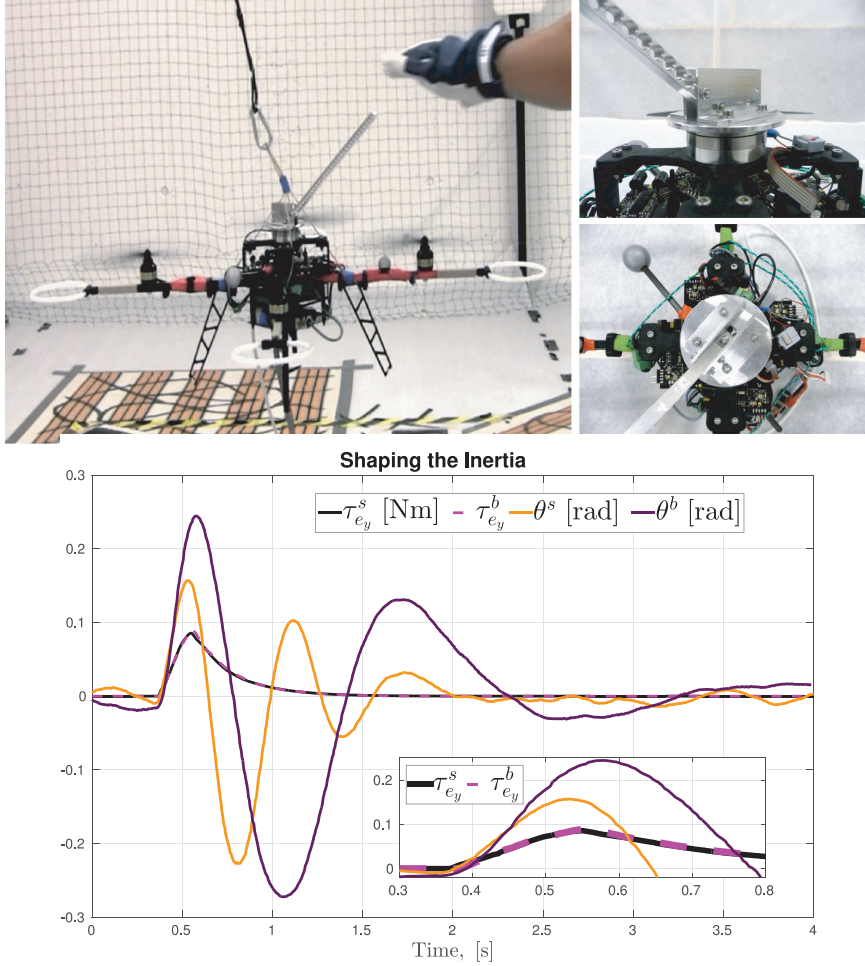


Fig. 7. Top: Quadrotor equipped with an F/T sensor (see details of the setup in Section 3.2) is about to be disturbed by an external interaction from the tip point of the rigid tool, during the hovering condition. For security reasons, a cable with no tension is connected to the system from the top. Bottom: System response (second-order rotational dynamics) to the external disturbances around the \mathbf{y}_B -axis. Two cases are compared: system with bigger desired inertia (denoted with superscript $*$) and system with smaller desired inertia (denoted with s). Our proposed controller is used to assign the desired inertial properties, together with a high-level position controller described in Section 4.3.

$$\theta_c = \frac{2\theta_c^{max}}{\pi} \arctan\left(\frac{\bar{\theta}_c}{2\theta_c^{max}}\right).$$

Then, the desired roll and pitch angles to steer the system to the desired \mathbf{x} and \mathbf{y} configurations are

$$\phi^* = \arctan(\phi_c), \quad \theta^* = \arctan(\theta_c). \quad (76)$$

Now, remember that in (22), we showed how one can change the desired attitude equilibrium $\boldsymbol{\eta}^* = [\phi^* \ \theta^* \ \psi^*]^T \in \mathbb{R}^3$, which shapes the desired potential energy of the system as, $V_d(\mathbf{q})$. Then using the desired attitude equilibrium ϕ^*, θ^* from (76), and ψ^* is chosen any arbitrary number, e.g., $\psi^* = 0$, and placing this desired potential energy \bar{V}_d in (22) and ultimately using in $V_d(\mathbf{q})$; we make sure that the IDA-PBC controller can steer the system to a desired $\mathbf{x}_W - \mathbf{y}_W$ configuration using the control input in (29), with the desired physical behavior we have assigned to it. Moreover, by choosing the high-level control input as

$\mathbf{u}_o = [u_{o_t} \ \mathbf{0}_{1 \times 3}]^T \in \mathbb{R}^4$, and implementing it in (29), we can let the quadrotor track a trajectory along the \mathbf{z}_W -axis with desired physical properties. A sketch of this control scheme is depicted in Figure 6 for fixing the ideas.

Remark 4. Note also from Figure 6 that the high-level control input \mathbf{u}_o is providing only the additional thrust input for tracking z_q^d and its derivatives. Other desired trajectories along the underactuated directions, i.e., \mathbf{x}_W and \mathbf{y}_W , are tracked using solely the control inputs generated by IDA-PBC, i.e., \mathbf{u}_i . However, to generate this input, we actively compute a new desired attitude $\boldsymbol{\eta}^*$, which is done using the near-hovering scheme presented in Section 4.3.

4.4. Shaping the inertia

As explained in Section 2.3, IDA-PBC is a powerful method for controlling the physical interaction of the quadrotor by shaping its physical properties, through

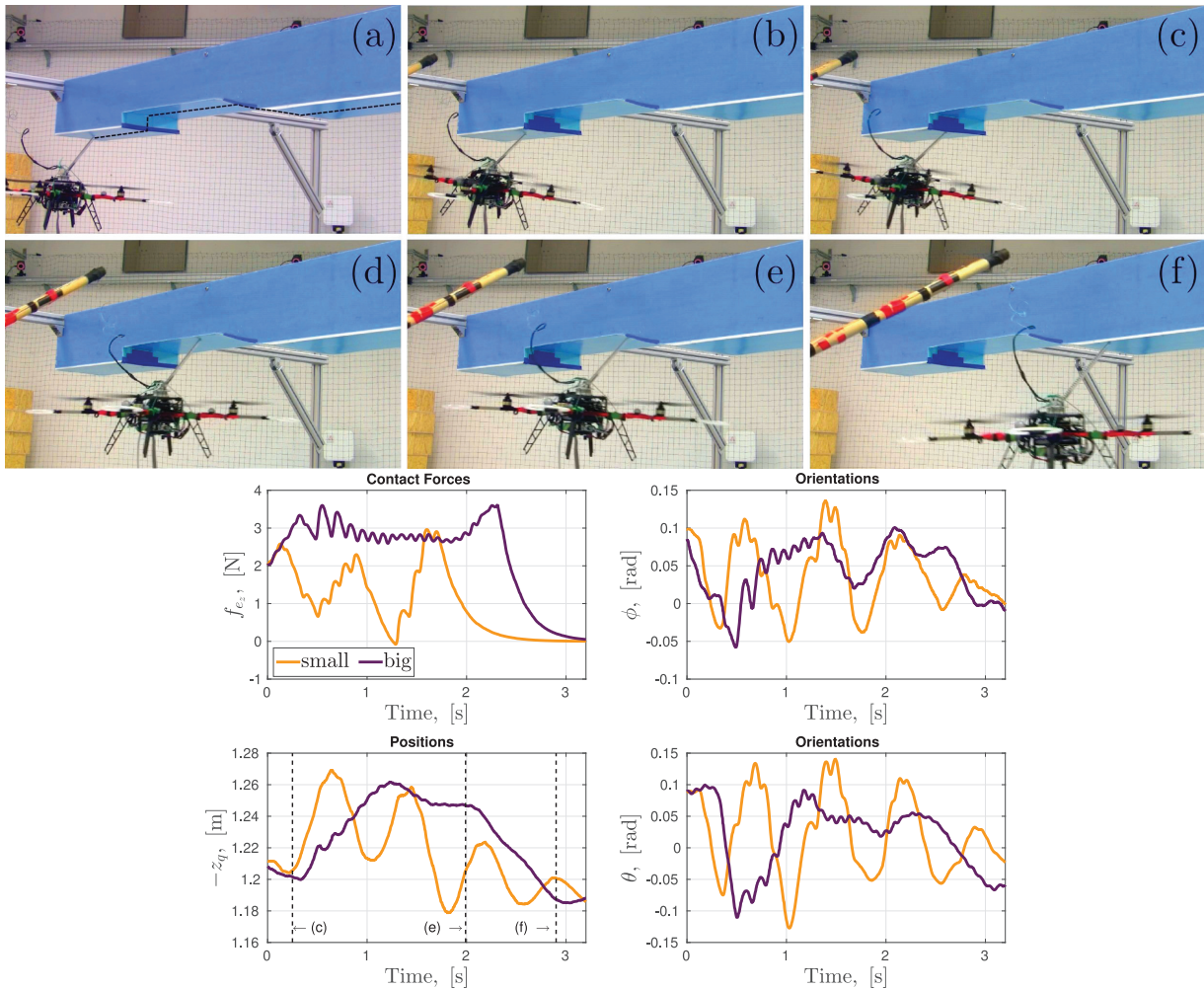


Fig. 8. Top: A series of snapshots (from (a) to (f)) from the experiments. The quadrotor setup as shown in Figure 4 is sliding on a blue-colored uneven ceiling surface. The tip of the rigid tool is in contact with the ceiling, and its bottom is rigidly attached to the F/T sensor and the quadrotor body frame. The overall system is secured with a *slack* cable connected to a stick, to avoid any dangerous crashes. Bottom: Experimental results for a quadrotor + rigid tool sliding on an uneven surface. Results for the system with the smaller desired inertia are depicted with gold curves, and the system with bigger desired inertia with purple curves. Three important time instants for z_q are highlighted with black dashed vertical lines; the moment before the dent (c), at the end of the dent and before the bulge (e), and the moment at the end of the bulge (f). Clearly, the system with bigger desired inertia follows the profile of the ceiling better than the one with the smaller desired inertia.

passivation. To test this in real experiments, we first bring the quadrotor to a hovering condition using the controller depicted in Figure 6. Then the flying system is disturbed with an external interaction on top of its tool tip, as shown in the top of Figure 7. We repeat this twice: first, the IDA-PBC controller is tuned for a smaller desired inertia (for the target dynamics) $\mathbf{N} = \text{diag}([0.008, 0.008, 0.0274]) \in \mathbb{R}^{3 \times 3}$, and then it is tuned for a bigger desired inertia $\mathbf{N} = \text{diag}([0.03, 0.03, 0.0274]) \in \mathbb{R}^{3 \times 3}$, only around the x_B - and y_B -axes. Remember from Figure 4 that the mass of the real system is $m = 1.49\text{kg}$, and its rotational inertia is $\mathbf{M}_{qr} = \text{diag}([0.01708, 0.0172, 0.0274]) \in \mathbb{R}^{3 \times 3}$.

The results are given on the bottom of Figure 7. For brevity, we only show the response of the second-order rotational dynamics to the external torque around the y_B -

axis. In the figure, superscript $*^s$ denotes the measurements of the *smaller desired inertia* case, whereas $*^b$ denotes the *bigger desired inertia* case. Note that the external torques for both cases (i.e., $\tau_{e_y}^s, \tau_{e_y}^b$, depicted with black solid and dashed magenta lines, respectively) are the same. However, the pitch orientations (i.e., θ^s, θ^b , depicted with gold and purple solid lines, respectively) are different from each other. Owing to the position tracker implemented together with IDA-PBC (see Figure 6), in both cases the quadrotor returns to its equilibrium after the disturbances. This creates a virtual rotational spring effect, making the system oscillate around its equilibrium until it reaches a region of attraction. Note the difference between the settling times of the two different cases; when the desired inertia is bigger, it takes longer for the

system to reach its steady state than when the desired inertia is smaller. This is in line with the fact that for a rotational mass–spring–damper system with constant spring,¹⁸ returning to its equilibrium would take longer when the rotational mass is greater.

This experiment and its results can be imagined for a human–robot physical interaction scenario, where we wish the flying robot to be able to physically interact with a human, and return to its equilibrium position as swiftly as possible. In such case one should aim at a flying robot with a smaller inertia than the original system has. Our controller provides here a controlled system with a desired physical interactive behavior.

4.5. Sliding on an uneven ceiling surface

Here we present some experimental results of the quadrotor + rigid tool setup, sliding on an uneven ceiling surface. The purpose of the experiments is to show that by reshaping the inertia of the system using our proposed method, we can change the performance of the APhI task, e.g., letting the quadrotor slide on the ceiling surface with a better contact profile.

The quadrotor + rigid tool setup is controlled using the method depicted in Figure 6, where the system is steered via joystick commands, which are provided by a human observer. Although the physical interaction is controlled autonomously, by bringing the human into the loop we aim at bringing some level of security to the system for avoiding an unexpected crash, and also pave the way for future human-in-the-loop experiments for APhI. The latter is especially in the scope of our future research, by considering the utilization of a haptic device, which allows bilateral control of the robot (see Franchi et al., 2012).

The results of the experiments are given in Figure 8. There, we compare two cases: quadrotor controlled with a small desired inertia, i.e., $\mathbf{N} = \text{diag}([0.004, 0.004, 0.0274]) \in \mathbb{R}^{3 \times 3}$, and with a big desired inertia, i.e., $\mathbf{N} = \text{diag}([0.014, 0.014, 0.0274]) \in \mathbb{R}^{3 \times 3}$. Note that the desired inertias are assigned only around \mathbf{x}_B - and \mathbf{y}_B -axes, whereas for the rotations around \mathbf{z}_B it is same as the original system. On the top of Figure 8 several snapshots from the experiments are given, where: (a) the quadrotor + rigid tool is first time in contact with the ceiling surface; (b) it is sliding on the even part of the ceiling; (c) just before the dent; (d) right after the dent; (e) just before a bulge which is built smoothly; (f) right after the bulge.¹⁹

The bottom of the figure shows the results, where gold solid curves show the response of the system with smaller desired inertia, and the purple solid curves for the system with bigger desired inertia. The contact forces acquired from the F/T sensor along the \mathbf{z} -axis are given as the first plot, and below it the z_q position of the quadrotor is shown. Two plots in the second column show the roll (ϕ) and pitch (θ) values. Note that the system with a bigger desired inertia (purple) preserves its contact with the ceiling much

better than that with a smaller desired inertia (gold), despite the uneven profile of the surface. A smaller desired inertia, in this case $\mathbf{N} = \text{diag}([0.004, 0.004, 0.0274]) \in \mathbb{R}^{3 \times 3}$, causes more oscillations for the system along the \mathbf{z}_W axis (z_q , up and down) and also around its rotational axes (see ϕ , θ). When we implement the controller to obtain a bigger desired inertia, i.e., $\mathbf{N} = \text{diag}([0.014, 0.014, 0.0274]) \in \mathbb{R}^{3 \times 3}$, these oscillations are reduced and the contact with the surface during sliding became much better (note especially the plot of the contact forces in Figure 8). This result is in line with the numerical simulations of both Yüksel et al. (2014b) and Yüksel et al. (2014a).

This experiment and its results can be interpreted as a robot–environment physical interaction scenario, where we wish the flying robot to slide on a ceiling surface, e.g., for cleaning or painting task. In such a case, we might wish for a flying robot with a greater inertia than the original system, and our proposed method can provide this while ensuring the passivity (with strong implication of stability) of the controlled system.

We note that in Figure 8, even when the system is controlled for a bigger desired inertia, some small oscillations appear during the contact. This can be further improved by shaping the dissipation of the system, changing, e.g., k_T , given in (26).

We refer the reader to Extension 1 for a better visualization of the experimental results.

5. Conclusions

In this paper, we have presented an IDA-PBC method for reshaping the physical properties of a quadrotor, a robustness analysis, and the first experimental results for different APhI tasks. For performing APhI, the controller requires knowledge of the external forces and torques, and in this paper we have implemented and discussed two methods: (indirect) estimation and (direct) measurement of the external wrenches. Although each method overcomes another for different reasons, we chose to use a lightweight low-cost 6D F/T sensor on board of a quadrotor for APhI, because of the results presented in Figure 5, and considering future outdoor APhI applications. To the best of the authors' knowledge, this is the first study of a quadrotor flying freely and performing an APhI task, with a 6D F/T sensor and its complete electronics on board of this flying platform. Moreover, for the first time we have presented the experimental results of controlling a quadrotor with IDA-PBC for APhI, in which the system is sliding on an uneven ceiling surface. This task can be interpreted in a later stage as surface inspection, painting, or cleaning.

There are several possible future extensions of this work. First, thus far we have not really taken advantage of the high-level control input \mathbf{u}_o , except in the way shown in Section 4.3. The employment of this control input for, e.g., F/T tracking or accounting for noise effects mentioned in Section 2.4 is in the scope of our future work. Furthermore,

looking at the results in Figure 8, the contact profile with an uneven surface during sliding can be further improved by changing the dissipative parameters, e.g., k_T , and also the desired mass m_d , but considering the limitations imposed by the robustness analysis from Section 2.4.

Funding

The author(s) disclosed receipt of the following financial support for the research, authorship, and/or publication of this article: This work has been also partially funded by the European Union's Horizon 2020 research and innovation programme (grant agreement number 644271 AEROARMS).

ORCID iD

Antonio Franchi  <https://orcid.org/0000-0002-5670-1282>

Notes

1. Potential energy is only one of the factors affecting the way a mechanical system interacts with the environment. Inertial properties and damping also play a major role for determining the interactive behavior. Furthermore, because the direction of the thrust of a quadrotor depends on the orientation of the system, it is not sufficient to shape the Cartesian impedance for achieving an effective control of interaction. In light of this, we improved this controller in Yüksel et al. (2014b), which is recalled and reformulated in Section 2.
2. Even though IDA-PBC has been extended to generic affine systems in Astolfi and Ortega (2009), starting from a PH dynamics is helpful for achieving simpler matching equations.
3. That is, it is a positive-definite differentiable energy function with a minimum at the desired equilibrium.
4. Note that the robustness of the pre-compensating control input in (8) was evidenced in Section III of Lee et al. (2013).
5. Clearly from (49), the noises on the other states do not affect the wrench compensating control input.
6. Note that the external wrench information acquired from different parts of the robot except its CoM can still be used for the IDA-PBC framework presented in Section 2 by applying rigid transformations. In addition, note that the control can also be reformulated for points of interest different than the CoM.
7. This implies the following: from the F/T sensor we get $\bar{\mathbf{w}}_s \in \mathbb{R}^6$ which is naturally given in the sensor body frame, \mathcal{F}_S . However, for our convenience we want to transform it into \mathbf{w}_s defined in \mathcal{F}_{Sb} , because it has the same orientation as the body frame of the quadrotor. To do so, we apply (70).
8. Note that if $\bar{\mathbf{d}}_l$ is the distance between P_T and P_S in \mathcal{F}_S , then according to Figure 3 it is true that $\mathbf{d}_l = \mathbf{R}_S^B \bar{\mathbf{d}}_l$, where $\bar{\mathbf{d}}_l = [0.2 \ 0 \ 0.15]^T$ m.
9. Note the zoomed grayed-out parts of the figure, which are clearly showing the superior performance of the F/T sensor measurements over the estimations. Although the estimation performance can be improved by better tuning, this would be a model-dependent approach, which might be a challenging task if the system is hard to model.
10. See <http://www.mikrokopter.de/en/home>
11. See http://wiki.mikrokopter.de/en/BL-Ctrl_2.0
12. See <https://git.openrobots.org/projects/tk3-mikrokopter>

13. See <http://robotpkg.openrobots.org/robotpkg/localization/pom-genom3/index.html>
14. See https://redmine.laas.fr/projects/byueksel/repository/ftsens_iit
15. See http://wiki.icub.org/wiki/FT_sensor
16. See https://svn.tuebingen.mpg.de/humus-telekyb/hydro/trunk/packages/telekyb_users/tk_byueksel/src/ftsens_subpub.cpp
17. See https://svn.tuebingen.mpg.de/humus-telekyb/hydro/trunk/packages/telekyb_users/tk_byueksel/
18. Note that the spring effect is due to the choice of the rotational desired inertia \bar{V}_d , damping is due to the damping injection implemented inside of the IDA-PBC, and the angular mass is the desired inertia \mathbf{N} .
19. Note that the experiments are performed in a limited environment, because the artificial ceiling we have built in-house has a limited size (1.73m in longitudinal direction). On the other hand, this was not the case for the simulations of Yüksel et al. (2014b), where the quadrotor was able to slide on a surface for a couple of hundred meters.

References

- Acosta JA, Sanchez MI and Ollero A (2014) Robust control of underactuated aerial manipulators via IDA-PBC. In: *2014 IEEE Conference on Decision and Control*, Los Angeles, CA, pp. 673–678.
- Astolfi A and Ortega R (2009) Dynamic extension is unnecessary for stabilization via interconnection and damping assignment passivity-based control. *Systems and Control Letters* 58(2): 133–135.
- Augugliaro F and D'Andrea R (2013) Admittance control for physical human-quadrocopter interaction. In: *12th European Control Conference*, Zurich, Switzerland, pp. 1805–1810.
- Bellens S, De Schutter J and Bruyninckx H (2012) A hybrid pose/wrench control framework for quadrotor helicopters. In: *2012 IEEE International Conference on Robotics and Automation*, St.Paul, MN, pp. 2269–2274.
- Cai G, Dias J and Seneviratne L (2014) A survey of small-scale unmanned aerial vehicles: Recent advances and future development trends. *Unmanned Systems* 2(2): 1–25.
- Chen W, Ballance DJ, Gawthrop PJ and O'Reilly J (2000) A nonlinear disturbance observer for robotic manipulators. *IEEE Transactions on Industrial Electronics* 47(4): 932–938.
- Fantoni I and Lozano R (2002) *Non-linear Control for Underactuated Mechanical Systems*. Berlin: Springer.
- Franchi A and Mallet A (2017) Adaptive closed-loop speed control of BLDC motors with applications to multi-rotor aerial vehicles. In: *2017 IEEE International Conference on Robotics and Automation*, Singapore, pp. 5203–5208.
- Franchi A, Secchi C, Ryll M, Bühlhoff HH and Robuffo Giordano P (2012) Shared control: Balancing autonomy and human assistance with a group of quadrotor UAVs. *IEEE Robotics and Automation Magazine* 19(3): 57–68.
- Fumagalli M, Ivaldi S, Randazzo M, et al. (2012a) Force feedback exploiting tactile and proximal force/torque sensing. *Autonomous Robots* 33: 381–398.
- Fumagalli M, Naldi R, Macchelli A, Carloni R, Stramigioli S and Marconi L (2012b) Modeling and control of a flying robot for contact inspection. In: *2012 IEEE/RSJ International Conference on Intelligent Robots and Systems*, Vilamoura, Portugal, pp. 3532–3537.
- Gioioso G, Ryll M, Prattichizzo D, Bühlhoff HH and Franchi A (2014) Turning a near-hovering controlled quadrotor into a 3D

- force effector. In: *2014 IEEE International Conference on Robotics and Automation*, Hong Kong, China, pp. 6278–6284.
- Grabe V, Riedel M, Bühlhoff HH, Robuffo Giordano P and Franchi A (2013) The TeleKyb framework for a modular and extendible ROS-based quadrotor control. In: *6th European Conference on Mobile Robots*, Barcelona, Spain, pp. 19–25.
- Guerrero ME, Mercado DA, Lozano R and Garcia CD (2015) Passivity based control for a quadrotor uav transporting a cable-suspended payload with minimum swing. In: *2015 IEEE Conference on Decision and Control*, Osaka, Japan, pp. 6718–6723.
- Ha C, Lee DJ and Nguyen HN (2015) Mechanics and control of quadrotors for tool operation. *Automatica* 61: 289–301.
- Khalil HK (2001) *Nonlinear Systems*. 3rd Ed. Englewood Cliffs, NJ: Prentice Hall.
- Lee DJ, Franchi A, Son HI, Bühlhoff HH and Robuffo Giordano P (2013) Semi-autonomous haptic teleoperation control architecture of multiple unmanned aerial vehicles. *IEEE/ASME Transactions on Mechatronics* 18(4): 1334–1345.
- Mahony R, Beard RW and Kumar V (2016) *Modeling and Control of Aerial Robots*. Berlin: Springer, pp. 1307–1334.
- McKinnon CD and Schoellig AP (2016) Unscented external force and torque estimation for quadrotors. In: *arXiv Preprint* 1603.02772.
- Mersha AY, Carloni R and Stramigioli S (2011) Port-based modeling and control of underactuated aerial vehicles. In: *2011 IEEE International Conference on Robotics and Automation*, Shanghai, China, pp. 14–19.
- Naldi R (2008) Prototyping, modeling and control of a class of vtol aerial robots. Doctorate Thesis, University of Bologna.
- Naldi R, Gentili L, Marconi L and Sala A (2010) Design and experimental validation of a nonlinear control law for a ducted-fan miniature aerial vehicle. *Control Engineering Practice* 18(7): 747–760.
- Nguyen H and Lee D (2013) Hybrid force/motion control and internal dynamics of quadrotors for tool operation. In: *2013 IEEE/RSJ International Conference on Intelligent Robots and Systems*, Tokyo, Japan, pp. 3458–3464.
- Nikoobin A and Haghghi R (2009) Lyapunov-based nonlinear disturbance observer for serial n -link robot manipulators. *Journal of Intelligent and Robotics Systems* 55(2–3): 135–153.
- Ortega R, van der Schaft A, Maschke B and Escobar G (2002) Interconnection and damping assignment passivity-based control of port-controlled Hamiltonian systems. *Automatica* 38(4): 585–596.
- Ruggiero F, Cacace J, Sadeghian H and Lippiello V (2014) Impedance control of VTOL UAVs with a momentum-based external generalized forces estimator. In: *2014 IEEE International Conference on Robotics and Automation*, Hong Kong, China, pp. 2093–2099.
- Schiano F, Alonso-Mora J, Rudin K, Beardsley P and Siciliano RB (2014) Towards estimation and correction of wind effects on a quadrotor UAV. In: *IMAV 2014: International Micro Air Vehicle Conference and Competition*, Delft, the Netherlands.
- Secchi C, Stramigioli S and Fantuzzi C (2007) *Control of Interactive Robotic Interfaces: A Port-Hamiltonian Approach (Tracts in Advanced Robotics)*. Berlin: Springer.
- Sepulchre R, Jankovic M and Kokotovic P (1997) *Constructive Nonlinear Control (Communications and Control Engineering Series)*. Berlin: Springer.
- Siciliano B and Khatib O (2008) *Handbook of Robotics*. Berlin: Springer.
- Spong MW (1998) Underactuated mechanical systems. In: B Siciliano and KP Valavanis (eds.) *Control Problems in Robotics and Automation*. Berlin: Springer, pp. 135–150.
- Tomic T and Haddadin S (2014) A unified framework for external wrench estimation, interaction control and collision reflexes for flying robots. In: *2014 IEEE/RSJ International Conference on Intelligent Robots and Systems*, pp. 4197–4204.
- Wang Z, Goldsmith P and Gu J (2009) Regulation control of underactuated mechanical systems based on a new matching equation of port-controlled Hamiltonian systems. In: *2009 IEEE International Conference on Robotics and Automation*, Kobe, Japan, pp. 992–997.
- Willems JC (1972) Dissipative dynamical systems part I: General theory. *Archive for Rational Mechanics and Analysis* 45(5): 321–351.
- Yu Y and Ding X (2012) A quadrotor test bench for six degree of freedom flight. *Journal of Intelligent and Robotics Systems* 68(3): 323–338.
- Yüksel B (2017) *Design, Modeling and Control of Aerial Robots for Physical Interaction and Manipulation*. Berlin: Logos Verlag.
- Yüksel B, Secchi C, Bühlhoff HH and Franchi A (2014a) A nonlinear force observer for quadrotors and application to physical interactive tasks. In: *2014 IEEE/ASME International Conference on Advanced Intelligent Mechatronics*, Besançon, France, pp. 433–440.
- Yüksel B, Secchi C, Bühlhoff HH and Franchi A (2014b) Reshaping the physical properties of a quadrotor through IDA-PBC and its application to aerial physical interaction. In: *2014 IEEE International Conference on Robotics and Automation*, Hong Kong, China, pp. 6258–6265.
- Zhan X (2006) Extremal eigenvalues of real symmetric matrices with entries in an interval. *SIAM Journal on Matrix Analysis and Applications* 27(3): 851–860.

Appendix. Index to multimedia extensions

Archives of IJRR multimedia extensions published prior to 2014 can be found at <http://www.ijrr.org>, after 2014 all videos are available on the IJRR YouTube channel at <http://www.youtube.com/user/ijrrmultimedia>

Table of Multimedia Extensions

Extension	Media type	Description
1	Video	Visualization of the experimental results